

UCGE Reports
Number 20143

Department of Geomatics Engineering

**Carrier Phase Based Ionosphere Recovery Over A
Regional Area GPS Network**

(URL: <http://www.geomatics.ucalgary.ca/GradTheses.html>)

by

Xiangqian Liao

September 2000



THE UNIVERSITY OF CALGARY

**CARRIER PHASE BASED IONOSPHERE RECOVERY OVER A
REGIONAL AREA GPS NETWORK**

by

Xiangqian Liao

A THESIS

SUBMITTED TO THE FACULTY OF GRADUATE STUDIES
IN PARTIAL FULFILLMENT OF THE REQUIREMENTS FOR THE DEGREE OF
MASTER OF SCIENCE

DEPARTMENT OF GEOMATICS ENGINEERING

CALGARY, ALBERTA

SEPTEMBER, 2000

©Xiangqian Liao 2000

ABSTRACT

A new approach of ionosphere recovery has been developed and described in this thesis using a regional area GPS network. The approach focuses on recovering ionosphere vertical TEC at centimetre accuracy using carrier phase as the principal observable. To eliminate possible satellite and receiver dependent biases, a double difference method has been employed from which the absolute ionosphere estimates are determined. A grid model has been developed along with a streamlined Kalman filter to model and estimate the vertical ionosphere TEC over the network. The performance of the proposed ionosphere recovery method has been tested using data from a regional GPS network currently in operation. The testing results have indicated that the regional ionosphere estimates are at the accuracy of several centimetres. A software package was developed to implement the proposed methodology.

ACKNOWLEDGEMENTS

I wish to show deep gratitude to Dr. Yang Gao, the author's supervisor, for his encouragement, guidance, and financial support during my graduate studies.

Special thanks also go to Dr. G. Lachapelle, Dr. S. Skone and Dr. K.P. Schwarz. The author has gained a lot from their teachings in GPS, atmosphere and INS.

I would also acknowledge Zhe Liu, Ron Ramseran and other members in the research group. Our close collaboration during the past years has made the work a pleasure. Thanks are also extended to Kevin Bourgue for his proofreading of this thesis.

I would like to appreciate Mr. G. Hedling for providing the SWEPOS data used in this thesis.

Finally, I would thank my fellow graduate students in this department: Jihong Zhang, Ning Luo, Huming Wu, Keong Gong, Chuanyun Fei, Yong Hu, and the others who have made our lives in Calgary colorful.

LIST OF CONTENTS

ABSTRACT.....	II
ACKNOWLEDGEMENTS.....	III
LIST OF CONTENTS	IV
LIST OF TABLES	VII
LIST OF FIGURES	VIII
LIST OF ACRONYMS.....	X
1 INTRODUCTION	1
1.1 BACKGROUND.....	1
1.2 OBJECTIVE.....	5
1.3 OUTLINE.....	6
2 GPS OBSERVABLE AND ERROR SOURCES	8
2.1 GPS OVERVIEW	8
2.2 GPS OBSERVABLE	9
2.3 GPS OBSERVABLE ERROR SOURCES	11
2.4 DIFFERENTIAL GPS	17
3 IONOSPHERE AND ITS EFFECTS ON GPS.....	20
3.1 PHYSICAL MECHANISM OF IONOSPHERE.....	20
3.1.1 <i>Physical Process</i>	20
3.1.2 <i>Ionosphere Layers</i>	21
3.1.3 <i>Sun Spots</i>	24
3.2 REFRACTIVE INDEX OF IONOSPHERE.....	25
3.3 IONOSPHERIC EFFECTS ON GPS	27
3.3.1 <i>Ionospheric Group Delay and Phase Advance</i>	28
3.3.2 <i>Total Electron Content</i>	29
3.3.3 <i>Geomagnetic and Ionospheric Storms</i>	30
3.3.4 <i>Ionospheric Scintillation</i>	31

3.4	GPS IONOSPHERE MODELLING.....	33
3.4.1	<i>Klobuchar Model</i>	33
3.4.2	<i>Dual-frequency Model</i>	34
3.4.3	<i>Modelling Over A WADGPS Network</i>	35
3.4.4	<i>Modelling Over A RADGPS Network</i>	40
4	CARRIER PHASE BASED IONOSPHERE RECOVERY USING A REGIONAL AREA GPS NETWORK.....	42
4.1	INTRODUCTION	42
4.2	DERIVATION OF IONOSPHERE MEASUREMENTS	43
4.3	A SINGLE LAYER IONOSPHERE GRID MODEL.....	45
4.4	A STREAMLINED KALMAN FILTER.....	48
4.4.1	<i>The Concept</i>	48
4.4.2	<i>Dynamic Model</i>	52
4.4.3	<i>Measurement Model</i>	53
4.4.4	<i>Sequential Filtering</i>	56
4.5	GRID SIZE AND OBSERVABILITY	59
5	REGIONAL AREA GPS NETWORK AMBIGUITY RESOLUTION	62
5.1	GPS ERROR REDUCTION.....	62
5.1.1	<i>Troposphere Error</i>	63
5.1.2	<i>Orbital Error</i>	66
5.1.3	<i>Reduced Phase Observable Equations</i>	68
5.2	DEVELOPMENT OF AN AMBIGUITY RESOLUTION ALGORITHM FOR REGIONAL AREA GPS NETWORKS	69
5.2.1	<i>Ambiguity Search Space</i>	69
5.2.2	<i>Ambiguity Candidate Discrimination</i>	72
5.2.3	<i>Ambiguity Constraints</i>	74
5.3	CARRIER PHASE CYCLE SLIP DETECTION.....	77
6	NUMERICAL RESULTS AND PERFORMANCE ANALYSIS.....	80
6.1	SOFTWARE DEVELOPMENT.....	80
6.2	TEST DATA DESCRIPTION.....	82
6.2.1	<i>SWEPOS Network</i>	82
6.2.2	<i>Satellite Availability</i>	85

6.3	CODE-DERIVED SLANT IONOSPHERE ANALYSIS	86
6.4	AMBIGUITY RESOLUTION RESULTS	88
6.5	PHASE-DERIVED DOUBLE DIFFERENCE IONOSPHERE MEASUREMENT ANALYSIS.....	90
6.5.1	<i>Phase-derived Double Difference Ionosphere</i>	90
6.5.2	<i>Comparison between Phase-derived and Code-derived Double Difference Ionosphere Measurements</i>	96
6.6	IONOSPHERE PIERCE POINT DISTRIBUTION	100
6.7	IONOSPHERE RECOVERY RESULTS AND ANALYSIS.....	101
6.8	PERFORMANCE ANALYSIS	104
7	CONCLUSIONS AND RECOMMENDATIONS	108
	CONCLUSIONS	108
	RECOMMENDATIONS	110
	REFERENCES	113

LIST OF TABLES

Table 6. 1: Ambiguity resolution summary from the whole network.....	89
Table 6. 2: Mean of the double difference ionosphere delay for all the baselines.....	96
Table 6. 3: RMS of the recovered double difference ionosphere.....	107

LIST OF FIGURES

Figure 3. 1:	Ionosphere layers and the corresponding electron densities.	23
Figure 3. 2:	Sunspot numbers and the periodic behaviors.....	25
Figure 3. 3:	Day-to-day variations of TEC in middle latitudes.....	30
Figure 4. 1:	Slant ionosphere path illustration.....	47
Figure 4. 2:	A regional area ionosphere grid model.....	49
Figure 4. 3:	Geomagnetic local hour angle of the pierce points for 3 GPS satellites... ..	50
Figure 4. 4:	Streamlined Kalman filter.....	50
Figure 4. 5:	A function model of double difference ionosphere measurement with the vertical TEC of the surrounding grid points.....	54
Figure 4. 6:	Typical maximum zenith difference.....	59
Figure 4. 7:	The tracks of pierce points for one visible satellite.....	60
Figure 4. 8:	The pierce points for all visible satellites in the solar-geomagnetic reference frame.....	61
Figure 5. 1:	Double difference ionosphere delay and troposphere residual.....	65
Figure 5. 2:	Double difference troposphere residual after modelling.....	65
Figure 5. 3:	Geometric range difference between precise and broadcast ephemeris. .	67
Figure 5. 4:	Difference between the double difference geometric ranges using precise and broadcast ephemeris.....	68
Figure 5. 5:	Accumulated sum of squared residual for correct ambiguity and incorrect ambiguity.....	74
Figure 5. 6:	Illustration of ambiguity search space.....	75
Figure 5. 7:	Misclosure ambiguity check.....	76
Figure 5. 8:	Typical GPS cycle slip on L1 phase.....	78
Figure 5. 9:	The corresponding Doppler on L1.....	79
Figure 6. 1:	Data processing flowchart of GNI software.....	81
Figure 6. 2:	SWEPOS GPS network.....	84
Figure 6. 3:	Baseline configuration.....	85

Figure 6. 4:	Number of the commonly visible satellites for the whole network.	86
Figure 6. 5:	Ionosphere delay without bias removed (m).....	87
Figure 6. 6:	Slant ionosphere delay (on L1) at Jonk (without L1/L2 instrumental bias removed), on May 17-18, 1999.....	88
Figure 6. 7:	Double difference ionosphere measurement for Jonk-Vane (159km).....	91
Figure 6. 8:	Double difference ionosphere measurements for Jonk-Kart (192km).....	92
Figure 6. 9:	Double difference ionosphere measurements for Jonk-Leks (335km).	92
Figure 6. 10:	Double difference ionosphere measurements for Jonk-Mart (366km).	93
Figure 6. 11:	Double difference ionosphere measurements for Jonk-Lovo (282km).....	93
Figure 6. 12:	Double difference ionosphere measurements for Jonk-Visb (257km).....	94
Figure 6. 13:	Double difference ionosphere measurements for Jonk-Oska (139km).....	94
Figure 6. 14:	Double difference ionosphere measurements for Jonk-Hass (185km).	95
Figure 6. 15:	Double difference ionosphere measurements for Jonk-Norr (159km).....	95
Figure 6. 16:	Comparison of carrier phase derived and pseudorange derived double difference ionosphere (1).	99
Figure 6. 17:	Comparison of carrier phase derived and pseudorange derived double difference ionosphere (2).	100
Figure 6. 18:	Geomagnetic latitude band of pierce points on ionosphere shell.....	101
Figure 6. 19:	Recovered vertical TEC in regional area (geomagnetic latitude range of 7.5 degrees).	102
Figure 6. 20:	Standard deviation of the vertical ionosphere delay (on L1).....	103
Figure 6. 21:	Recovered vertical TEC in regional area (geomagnetic latitude range of 13.5 degrees).	103
Figure 6. 22:	Error distribution of the ionosphere estimates.	107

LIST OF ACRONYMS

C/A code	Coarse/Acquisition code
CONUS	CONTinental United States
DGPS	Differential GPS
DoD	Department of Defense
GPS	Global Positioning System
IGS	International GPS Service
LADGPS	Local Area Differential GPS
MCS	Master Control Station
NAVSTAR	NAVigation Satellite Timing And Ranging
P code	Precise code
RADGPS	Regional Area Differential GPS
ROTI	Rate Of TEC Index
RTCM	Radio Technical Commission Maritime Services
RTK	Real-Time Kinematic
SA	Selected Availability
SH	Spherical Harmonics
SPS	Standard Positioning Service
TEC	Total Electron Content
UTC	Universal Time Coordinated System
WAAS	Wide Area Augmentation System
WADGPS	Wide Area Differential GPS

CHAPTER 1

INTRODUCTION

1.1 BACKGROUND

Global Positioning System (GPS) is a satellite navigation system developed by US Department of Defense (DoD). The satellite constellation consists of 24 satellites in space, which broadcast navigation messages and provide global 24-hour all weather navigation service. Since its full operation in 1993, GPS has found a wide range of applications far beyond its initial purpose primarily for US military applications. Currently, GPS is increasingly used in the worldwide civilian community not only for air, marine, land navigation, but also for precise time transfer and geodetic surveys [Parkinson, 1994].

As a radio navigation system, GPS is subject to the effects of a number of error sources such as ionospheric and tropospheric errors, orbital error, multipath, clock biases, and measurement noise. Among them, ionosphere error is the largest one after SA (Selected Availability) was turned off on May 1, 2000. The ionosphere creates a delay in the received signal which can range from several metres to more than one hundred metres [Parkinson, 1994]. This will seriously corrupt the positioning and time transfer results unless these effects are taken into account. To mitigate the ionosphere effect, a number of ionosphere modelling methods have been developed including single frequency

Klobuchar model, dual-frequency correction, differential method, and network modelling. Each of these methods is appropriate in certain situations.

For stand-alone GPS positioning, Klobuchar model or the dual-frequency method can be used depending on the receiver type. The Klobuchar ionosphere model is derived from the empirical knowledge of the long-term ionosphere behavior. It is designed for single frequency users in which the required model parameters are broadcast via the navigation message from the satellites. This model is typically accurate to a few metres along the vertical direction at mid-latitude [Klobuchar, 1987].

The dual-frequency method is based on the dispersive property of the ionosphere and requires the use of a dual-frequency GPS receiver. When dual-frequency GPS observations are available, they can be used to derive the first-order ionosphere delay which can in return be subtracted from the original observations to remove its effect.

Differential GPS (DGPS) is another method that can be used to remove or reduce the ionosphere effects. In DGPS, corrections are generated at a base station and then provided to the remote users to reduce the spatially correlated errors such as ionosphere, troposphere and satellite ephemeris errors. In addition, the satellite or receiver clock errors can also be cancelled out by differencing between two receivers or two satellites respectively. Therefore, DGPS can provide high accuracy after the significant reduction of those errors. If carrier phase observable is used, centimetre-level accuracy can be achieved in some specific scenarios [Lachapelle et al., 1992]. DGPS however works

effectively only in local areas within, for instance, 50 kilometres. Therefore, conventional local area DGPS method can't be used for large area DGPS applications. Furthermore, it is also not cost-effective to implement a large number of such independent reference stations to achieve a large area coverage. Because of this, Wide Area Differential GPS (WADGPS) and Regional Area Differential GPS (RADGPS) methods become popular in recent years which can overcome the drawbacks associated with the conventional DGPS method.

A WADGPS network includes a number of widely distributed reference stations with baselines typically in the range of several thousand kilometres, each of which is equipped with a GPS receiver (usually dual-frequency) and communication equipment. In this case, the ionosphere is monitored using the GPS observations from all the reference stations. The ionosphere corrections are then produced over the covered area by some appropriate models such as grid-model, spherical harmonics, polynomial fitting [El – Arini et al., 1994]. Extensive research has been done in this area and the resulting ionosphere correction accuracy can be achieved at sub-metre level under minimum solar conditions [i.e. Mannucci et al., 1993; Wu et al., 1996].

As more and more permanent GPS stations, managed by International GPS Service (IGS), are setup around the world in recent years, ionosphere research is extended to global-scale [IGS Central Bureau annual report, 1996]. The operating IGS stations keep continuous satellite tracking using high precision receivers, and the collected data is archived and distributed to satisfy a wide range of applications and experimentation. IGS

GPS network data have been used by the IGS analysis centers to generate products such as ionospheric and tropospheric corrections, precise GPS ephemeris, precise GPS satellite and receiver clock corrections, as well as Earth rotation parameters. The processing results from different IGS data analysis centers are also regularly assembled for comparisons and further analysis.

A RADGPS network consists of regionally distributed reference stations with baselines typically in the range of several hundred kilometres and can also be employed to create ionosphere corrections for the users within that region. RADGPS is very similar to a WADGPS network in concept but with a relatively smaller coverage size while having a much denser reference station distribution. In the past few years, GPS positioning using RADGPS networks [i.e. Wübbena et al., 1996; Komjathy and Langley, 1996; Wanninger, 1997; Varner and Cannon, 1997; Raquet et al., 1998] has attracted wide attention within the GPS community. The existing RADGPS ionosphere modelling algorithms have been focused on the estimation of the spatially correlated errors at the user sites using various interpolation methodologies. The corrections at the user sites can help facilitate the carrier phase ambiguity resolution and improve the positioning accuracy in Real-Time Kinematic (RTK) situations. In Gao and Li [1997, 1998], two different algorithms have been proposed to determine the ionospheric corrections at the user site using a regional area GPS network. The obtained results, however, have indicated that an integration of ionospheric measurements over time is required in order to improve the accuracy of the predicted ionosphere corrections to a centimetre level. A new model therefore, is required to satisfy such a need. Compared to WADGPS, GPS stations within a regional area are

more densely configured and the baseline length usually ranges from several tens kilometres to several hundred kilometres. The moderate baseline length in a RADGPS network therefore allows for the use of carrier phase instead of pseudorange as the principal observable if ambiguity resolution can be resolved using some appropriate methods. It is expected that the accuracy of the vertical TEC (Total Electron Content) derivations can be significantly improved in this case. In addition, the dense reference station configuration will improve the spatial resolution of ionosphere recovery. Investigating and developing effective RADGPS ionosphere recovery method thus becomes the subject of this thesis.

1.2 OBJECTIVE

The major objective of this thesis is to investigate a new ionosphere modelling and estimation method based on a regional area GPS network capable of providing precise regional ionosphere corrections to support decimetre or centimetre accurate DGPS positioning and navigation. Described below are the three specific objectives for this research:

- 1) Develop a new carrier phase based ionosphere estimation model using a regional area GPS network.
- 2) Develop a complete software package to implement the proposed method.
- 3) Test the performance of the proposed ionosphere recovery model using data from an operational regional area GPS network.

1.3 OUTLINE

This thesis is composed of seven chapters. Background and research objectives are included in Chapter 1.

In Chapter 2, an overview of GPS is provided with an emphasis on the analysis of different error sources including ionosphere error, troposphere error, orbit error, clock biases, multipath, and SA.

In Chapter 3, fundamental concept of ionosphere is introduced but the focus is placed on its effects on GPS. The basic physical characteristics of ionosphere are first presented, followed by its effects on GPS observations. A review of several ionosphere correction methods is provided in the latter part of this chapter.

Described in Chapter 4 is a new grid-based ionosphere model using carrier phase as the principal observable based on a regional area GPS network. The proposed methodology will include several components including a single layer regional area ionosphere recovery model, streamlined Kalman filter, and system observability. The detailed implementation of the ionosphere recovery model will be presented in this chapter.

Chapter 5 discusses the ambiguity resolution method proposed for the regional area ionosphere recovery. Different from the case of short baseline, the ambiguity search

space is defined using only carrier phase observations. Wide-lane ambiguity resolution and misclosure check are also conducted to aid the L1 and L2 ambiguity resolution.

Chapter 6 presents the testing results based on the methods given in Chapter 4 and Chapter 5 using data sets from a regional area GPS network. The numerical results are analyzed and the estimation accuracy is then assessed to confirm the efficiency of the developed ionosphere recovery method.

Chapter 7 summarizes the whole research work with conclusions and recommendations.

CHAPTER 2

GPS OBSERVABLE AND ERROR SOURCES

2.1 GPS OVERVIEW

NAVigation Satellite Timing And Ranging (NAVSTAR) GPS is a satellite navigation system capable of providing accurate, continuous global positioning and navigation services. The system consists of 24 operational satellites in space. With four to twelve satellites visible at any time and any place, the receiver can provide twenty-four-hour, all-weather, worldwide position, velocity and timing information [Wooden, 1985].

The GPS satellites transmit on two L-band frequencies with one at 1575.42 MHz (L1) and the other at 1227.60 MHz (L2). Each carrier is modulated by a 10.23Mb/s Precise code (P code) and a data message. The latter contains the satellite ephemeris, clock corrections and ionospheric correction parameters. In addition, L1 is modulated with a 1.023Mb/s pseudorandom bit sequence called Coarse/Acquisition code (C/A code). The C/A code is for civilian users, while the P code is encrypted to be accessed only by military and other authorized users [Hofmann-Wellenhof et al., 1994].

GPS uses the World Geodetic System WGS-84 as its reference coordinate system. The users' coordinates are determined in this frame and then can be further transformed to other systems such as local coordinate systems. The GPS time uses an atomic time scale. It was coincident with Universal Time Coordinated (UTC) system at the GPS standard

epoch of January 6, 1980. Due to the leap second of UTC, there is an offset between GPS and UTC time.

2.2 GPS OBSERVABLE

The observation types provided by GPS receivers depend on the different techniques used in the GPS receivers. The single frequency receiver can only output observations on L1 frequency, while some semi-codeless or codeless receivers can provide observations on dual frequencies. In any case, there are three basic types of observations, namely, pseudorange, carrier phase and Doppler measurements.

Pseudorange

The pseudorange measurement is the time difference (in equivalent metres) between the received signal and the receiver-generated signal. Since the measurement is not the true geometric range between the satellite and the receiver but significantly biased by receiver clock errors, it is consequently denoted as pseudorange. The observation equation can be expressed as:

$$P = r + c \cdot (dt - dT) + d_r + d_{trop} + d_{ion} + c \cdot \frac{f_1^2}{f_i^2} (T_{GD,r} - T_{GD,s}) + d_{mult/P} + e_P \quad (2.1)$$

where r is the geometric range;

- dt is the satellite clock error including SA;
- dT is the receiver clock error;
- d_r is the orbital errors (nominal and SA);
- d_{ion} is the ionosphere delay;
- d_{trop} is the troposphere delay;
- $T_{GD,r}$ is the receiver modulation offset;
- $T_{GD,s}$ is the satellite modulation offset;
- $f_i (i = 1, 2)$ is the satellite broadcast frequency on L1 or L2;
- $d_{mult/P}$ is the pseudorange multipath effect; and
- e_P is the pseudorange measurement noise.

Carrier phase

Carrier phase observation is the measured phase difference between the received signal and the receiver-generated signal. It can be expressed as:

$$\Phi = \mathbf{r} + c(dt - dT) + \mathbf{I}N + d_r + d_{trop} - d_{ion} + d_{mult/\Phi} + \mathbf{e}_\Phi \quad (2.2)$$

- where \mathbf{I} is the wavelength of GPS signal;
- N is the integer ambiguity of carrier phase;
- $d_{mult/\Phi}$ is the carrier phase multipath effect; and
- \mathbf{e}_Φ is the carrier phase measurement noise.

The remaining terms are defined as in the code pseudorange observable in Eq. (2.1). Comparing Eq. (2.1) and (2.2), we note that in order to utilize the carrier phase measurements, the integer phase ambiguities must be resolved.

Doppler observable

Doppler frequency is the change rate of the carrier phase observable. It reflects the relative velocity between the receiver and the GPS satellite. This information can be used for velocity derivation and cycle slip detection. The Doppler observable can be expressed as

$$\dot{\Phi} = \dot{r} + c(\dot{d}_i - \dot{d}_T) + \dot{d}_r + \dot{d}_{trop} - \dot{d}_{ion} + \dot{d}_{mult} / \Phi + \dot{\epsilon}_{\Phi} \quad (2.3)$$

where $\dot{\Phi}$ is the phase rate of carrier phase;

\dot{r} is the range rate between the receiver and the satellite.

The remaining terms are defined as the change rates of the corresponding terms in carrier phase observable in Eq. (2.2).

2.3 GPS OBSERVABLE ERROR SOURCES

As indicated in Eq. (2.1), (2.2) and (2.3), the GPS measurements are subject to many error sources, which degrades the obtainable accuracy of GPS positioning. These error sources are briefly reviewed below.

Ionosphere error

The ionospheric delay in GPS pseudorange observations is the second largest error source after SA. This delay can reach a 50ns range during periods of high solar activity at the zenith direction, and induces a vertical ranging error of about 15 metres [Klobuchar, 1996]. The delay would become 3 times as much when a satellite is close to the horizon. An ionospheric advance of equal magnitude and opposite sign is imposed on the GPS carrier phase observable. Details on the ionospheric effects and the corresponding methods of reduction will be discussed in later chapters.

Troposphere delay

The lower part of the atmosphere, called the troposphere, is electrically neutral and non-dispersive for frequencies as high as about 15 GHz. Within this medium, group and phase velocities of the GPS signal on both L1 and L2 frequencies are equal. The resulting delay is a function of atmospheric temperature, pressure, and moisture content. Without appropriate compensation, tropospheric delay will induce pseudorange and carrier-phase errors from about 2 metres for a satellite at zenith to more than 20 metres for a low-elevation satellite [Spilker, 1996].

Many geophysicists have developed a number of algorithms for the prediction of the tropospheric delay [i.e. Hopfield, 1970; Black and Eisner, 1984; Saastamoinen, 1973; Niell, 1996]. For most of the models, the atmosphere is assumed both horizontally

stratified and azimuthally symmetric. The tropospheric delay is modelled as the sum of two components: a hydrostatic component associated with primarily the dry molecular constituents of the atmosphere, and a non-hydrostatic (primarily wet component) associated with the water vapor in the atmosphere. Mathematically, it can be expressed by

$$d_{trop} = d_{hyd}^z \cdot m_{hyd} + d_{wet}^z \cdot m_{wet} \quad (2.4)$$

where d_{trop} is the total troposphere delay, d_{hyd}^z and d_{wet}^z are the hydrostatic and wet zenith delays, m_{hyd} and m_{wet} are the corresponding mapping functions which are used to map the zenith delay to the slant signal direction.

Orbital error

Three types of data are available to determine position and velocity vectors of the satellites in a terrestrial reference frame at any instant: almanac, broadcast ephemerides, and precise ephemerides [Hofmann-Wellenhof et al., 1994]. These data types differ in accuracy.

The purpose of the almanac is to provide the user with less precise data to facilitate satellite searching in the receiver or to plan tasks such as computation of visibility charts.

The almanac is about several kilometres in accuracy depending on the age of the data, it is updated at least every six days and broadcast as part of the satellite message.

The broadcast ephemerides are based on observations at the five monitor stations of the GPS control segment. The most recent collection of these data is used to compute the satellite ephemerides at the Master Control Station (MCS). The ephemerides are then uploaded to the satellites. These orbital data could be accurate to approximately 5m or even better.

The most accurate orbital information is provided by the IGS with a delay of about two weeks; rapid information is available about two days after the observations. Currently, IGS data and products are free of charge for all users. The precise ephemerides consist of satellite positions and velocities at an updating interval of 15 minutes. The position and velocity vectors at any given epoch can be obtained using an interpolation method. The final precise orbit data can be accurate at the level of 5 centimetres.

Satellite clock error

GPS satellites use two types of atomic clocks: rubidium and cesium. Satellite clock error is referred to as the difference between the satellite clock and the GPS system time. The satellite clock drift is described by the broadcast coefficients as part of the satellite navigation message. This kind of error is generally less than 1ms. Under the condition of SA, the satellite clock is dithered and the true behavior of the clock cannot be represented

by the broadcast coefficients. However, the incurred extra delay on the pseudorange or carrier phase measurements can be eliminated by differencing between two receivers with respect to the same satellite.

Receiver clock error

Receiver clock error is the offset between the receiver clock and the GPS system time. The error magnitude is a function of the receiver's internal firmware, e.g. the type of oscillator used in the receiver. The receiver clock error leads to a range error in the pseudorange and carrier phase measurements. Similar to the satellite clock error, the receiver clock error can be eliminated by differencing between the observations observed in a receiver between two different satellites.

Multipath error

Multipath is the corruption of the direct GPS signal by one or more signals reflected from the local surroundings. These reflections affect both code and carrier based measurements in a GPS receiver. Usually the signals received from low satellite elevations are more susceptible to multipath than those from high elevations. Pseudorange multipath is much greater than carrier phase multipath and it is typically on the order of several metres, whereas carrier phase multipath is on the order of a few centimetres. Carrier phase multipath is a limiting error source for high precision GPS applications such as attitude determination and short baseline surveying, in which the errors can be as much as several centimetres.

Multipath can be eliminated or reduced by selecting an antenna that has a specific property of signal polarization, using an antenna with radio absorbent chokering ground plane, or by using narrow correlation techniques in the receiver. The most effective counter-measure is to avoid sites where it could cause such a problem.

Measurement noise

The receiver noise level is dependent on a number of factors. For instance, it is usually a function of code correlation method, receiver dynamics and antenna gain pattern. With narrow correlation techniques, the measurement noise is at a level ranging from 0.1% to 1% of the measurement wavelength. The noise on pseudorange is at a level of tens of centimetres, while only several millimetres on carrier phase observable [Van Dierendonck et al., 1992].

Selected Availability (SA)

Selective Availability was the intentional degradation of GPS signals by the US Department of Defense (DoD). The goal of SA is to deny the navigation accuracy to potential adversaries. SA is implemented by d -process and e -process [Georgiadou and Doucet, 1993].

The **d**-process is achieved by dithering the fundamental frequency of the satellite clock. The resulting pseudorange and carrier phase observations are affected in the same way by a same amount of offset. By difference between two receivers with respect to the same satellite, the dithering effect can be eliminated. The **e**-process is implemented by truncating the orbital information in the transmitted navigation message resulting in a degradation of the computed coordinates of the satellites.

Following the specifications of the US DoD, the GPS positioning accuracy under SA is degraded to 100m for horizontal position and to 156m for height. These specifications also imply a velocity error of 0.3m s^{-1} and a time error of 340ns. All numbers are given at the 95% probability level. At the 99.99% probability level, the predictable accuracy decreases to 300m for horizontal position and to 500m for height [Department of Defense, 1993]. However, the military effectiveness of SA is undermined by some countermeasure alternatives such as differential techniques. According to the public announcement from the U.S. government, SA has been turned off since May 2, 2000. The standard positioning accuracy is improved to 5 ~ 15m at the 95% probability level.

2.4 DIFFERENTIAL GPS

Standard Positioning Services (SPS) provides GPS users with a horizontal accuracy of one hundred metres. To improve the positioning accuracy, differential GPS technique must be applied [Kalafus et al., 1984]. The idea behind all differential positioning

techniques is to correct range errors at the user location with measured range errors at reference station with known coordinates.

GPS corrections are often transmitted in RTCM SC-104 format specified by the Radio Technical Commission Maritime Services (RTCM) [Kalafus, 1986], whereas the transmission approach can be different. The U. S. Coast Guard maintains a network of differential monitor stations and transmits DGPS corrections over radio beacons covering much of the U. S. coastline, while some private DGPS services use leased FM sub-carrier broadcast or satellite links. The positioning accuracy using DGPS can be achieved at 1-10 metres using pseudoranges in real-time navigation. For differential positioning at centimetre accuracy, double difference static and kinematic techniques should be employed using carrier phase as the principal observable over short baselines. A millimetre level of positioning accuracy can also be obtained in static surveying [Hofmann-wellenhof et al., 1994].

Single reference DGPS can only apply within a relatively small range because the reference and remote receivers have to be close enough in order to ensure the similar atmospheric effects on the observations at both base and rover stations. To extend the differential services in a large area or even in a global range, a GPS network can be setup to generate the differential corrections. WADGPS and RADGPS are such kind of networks, in which the differential corrections are estimated using data from all reference stations within the network. The differential corrections include ionosphere parameters, clock corrections and orbit corrections [Kee and Parkinson, 1996].

In the past, GPS was primarily used for positioning, navigation, surveying and timing. However, GPS has also been proven as a useful tool to investigate the atmosphere above the Earth [Kursinski, 1994]. Since GPS signal penetrates the atmosphere before it arrives at the receiver, the received signal holds useful information of the atmosphere which can be used to determine properties of the atmosphere. The results from the GPS/STORM [Duan, et al., 1996] and GPS/MET [Ware et al., 1996] experiments have demonstrated that GPS can be used to monitor the ionosphere and troposphere. GPS has become an important information source in support of weather prediction and climate research.

CHAPTER 3

IONOSPHERE AND ITS EFFECTS ON GPS

This chapter will review some of the ionosphere characteristics, such as the physical process of ionosphere activities and their effects on GPS. Several ionosphere calibration techniques that have been used in GPS applications will also be reviewed.

3.1 PHYSICAL MECHANISM OF IONOSPHERE

The name “ionosphere” was proposed by R.A. Watson-Watt in 1926, and came into common use after 1930’s [Rishbeth and Garriott, 1969]. Since that time the ionosphere has been extensively studied and most of its principal features, though not all, are now fairly well understood in terms of the physical and chemical processes.

3.1.1 Physical Process

Invisible layers of ions and electrons are suspended in the Earth's atmosphere above about 60 kilometres in altitude. The main source of these layers is the Sun's ultraviolet light which ionizes atoms and molecules in the Earth's upper atmosphere [Bugoslavskaya, 1962]. During this process of photoionization, the electrons are released from the neutral atmospheric particles, which then become the ions. Because the Sun's light is responsible for most of the ionization, the electron density of the ionosphere reaches the maximum just after the local noon, with about one in every 1000 air particles

ionized. The resulting ionospheric density is about one million ions and electrons per cubic centimetre.

Ions and electrons in the ionospheric layer are constantly being lost and replenished. The lifetime of a given ion is only a fraction of a day and decreases with decreasing altitude. Lower altitude ions have shorter lifetimes. The low-altitude portion of the ionosphere (the D and E-layers in Figure 3.1) rapidly reaches the low densities at night time because ion and electron lifetimes are very short at these altitudes and the major source of new ion-electron pairs (solar photons) is absent.

Flares and other energetic events on the Sun produce increased ultraviolet, x-ray and gamma-ray photons that dramatically increase the density of the ionosphere on the dayside after arrival at the Earth. Some high velocity protons and electrons precipitate into the ionosphere in the polar region and cause large increases in the density of the ionosphere at polar and auroral altitudes.

3.1.2 Ionosphere Layers

The typical vertical structure of the ionosphere is shown in Figure 3.1. It should be noted that the various layers are not separated by distinct boundaries. The main regions are categorized into different layers including D, E, F1 and F2 [Rishbeth and Garriott, 1969]:

The D region is the ionosphere region above 60 km and below about 90 km. The density of charged particles ranges from 10^8 to 10^{10} m^{-3} in the daytime. This region will vanish at night due to the combination of the ions and electrons. The ions are formed by the ionization of atmospheric neutrals by hard X-ray radiation and solar Lyman α radiation. Due to the relatively high ambient atmospheric pressure, many negative ions are produced by electron attachment to atomic and molecular neutrals. Free electrons increase as the altitude increases.

The E region lies between 90 and 150 km above the Earth. The maximum electron density averages at about several 10^{11} m^{-3} in the daytime and 10^{10} m^{-3} at night. Ions in this region consist of O_2^+ , produced by direct absorption of solar radiation, and NO^+ , formed by charge transfer collisions with other ions (O^+ , O_2^+ , N_2^+) ionized by coronal X-rays. The normal E region, produced mainly by solar soft X-rays, has minimal effects on GPS. An intense E region, with irregular structure, produced by solar particle precipitation in the auroral region, might cause scintillation effects.

The region above about 150 km is known as F region. This region is usually divided into F1 and F2 sub-regions. The maximum electron density of the F1 region is a few times 10^{11} m^{-3} at about 200 km altitude. Due to dissociative recombination, the F1 region disappears at night. The electron density of the F2 region varies from 10^{11} to 10^{12} m^{-3} between day and night with the maximum at roughly 350 km. This peak is highly variable depending upon daily, seasonal, and sunspot-cycle variations. It should be noted that even at this maximum, the charged particle number density is much less than the

number density of neutral atmospheric gas (e.g. 10^{12} m^{-3} for electron density and 10^{15} m^{-3} for neutral particle density). The F region is formed by ionization of atomic oxygen by Lyman emissions and by emission lines of He. In the lower part of the F region, O^+ ions readily transfer charge to neutrals, forming NO^+ . In the F2 region, O^+ remains the dominant ion.

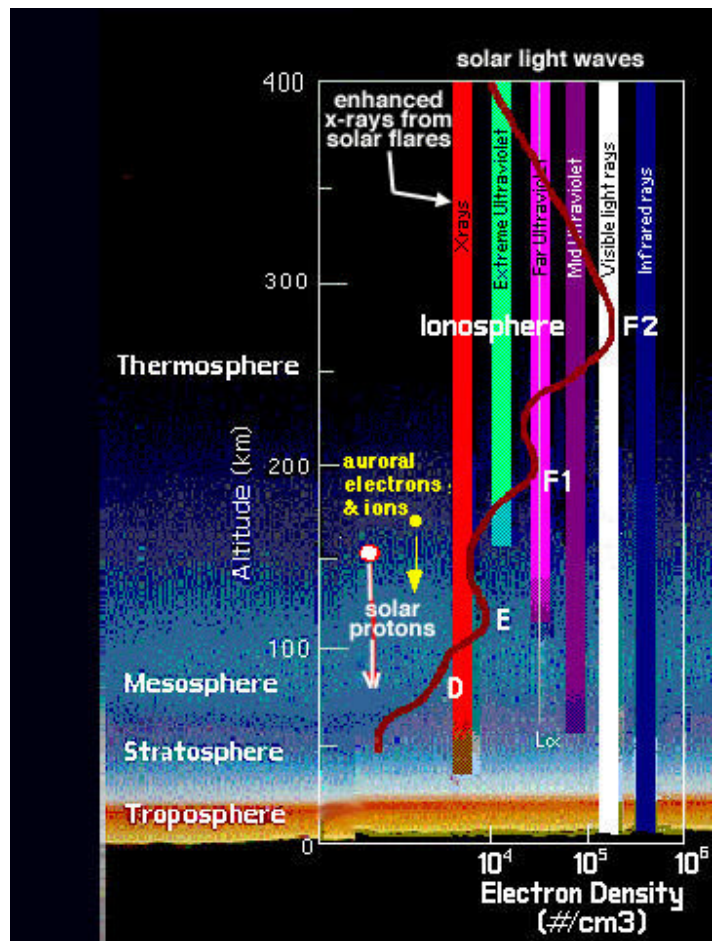


Figure 3. 1: Ionosphere layers and the corresponding electron densities.

(After

http://windows.engin.umich.edu:80/spaceweather/images/formation_ionosphere_jpg_image.html)

3.1.3 Sun Spots

The activity of the ionosphere is strongly affected by the number of the sunspots. The sunspots are dark patches on the Sun and they are always seen in pairs or in groups of pairs. Here the magnetic fields, as strong as those of a horseshoe magnet (which is about 1000 times stronger than the Earth's surface magnetic field), keep heat from flowing up to the surface, thus making the sunspots the coolest places on the Sun and accounts for its dark appearance. The Sun's differential rotation, faster at lower than higher latitudes, is critical in producing sunspots. Solar flares (enormous explosive releases of energy from the Sun) are most likely to occur in sunspot groups when they are growing rapidly and rotating, much like a hurricane. The number of sunspots on the Sun at any given time varies in an 11-year cycle as does the number and severity of disturbances in space weather [Bugoslavskaya, 1962]. Figure 3.2 shows the sunspot numbers in the history of 1750 ~ 1998. Constantly monitoring the development of sunspot groups is one important job of space weather forecasters, especially when the ionospheric activities are reaching the maximum in the middle of 2000.

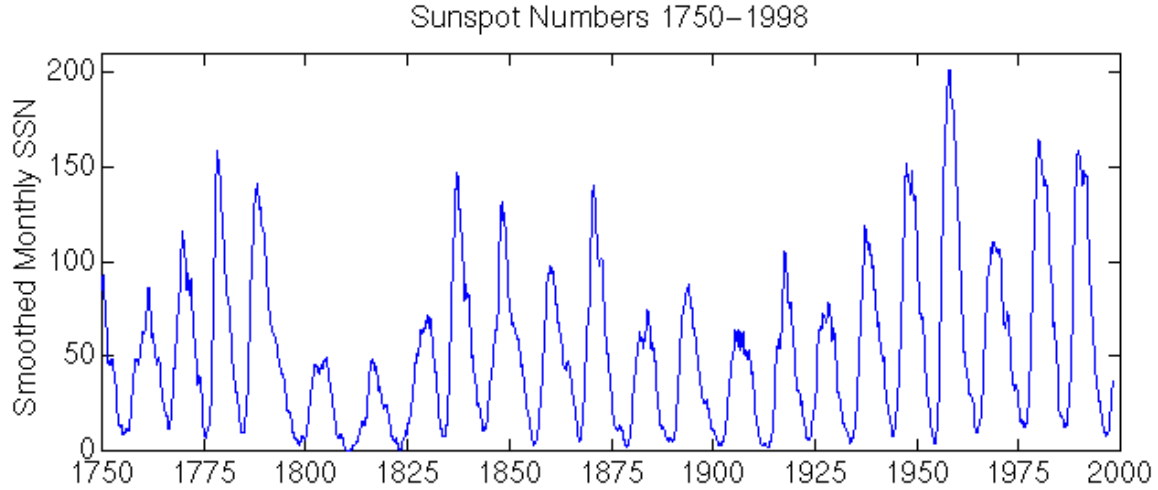


Figure 3. 2: Sunspot numbers and the periodic behaviors.

(After <http://www oulu.fi/~spaceweb/textbook/cycle.html>)

3.2 REFRACTIVE INDEX OF IONOSPHERE

The refractive index is one of the most important parameters to characterize the atmosphere. To examine the propagation effects on the radio signal travelling through the ionosphere, the refractive index of the medium must be specified. Based on the work of Appleton and Hartree [Davies, 1989], the phase refractive index n_p of the ionosphere can be expressed as

$$n_p^2 = 1 - \frac{X}{1 - iZ - \frac{Y_T^2}{2(1 - X - iZ)} \pm \left[\frac{Y_T^4}{4(1 - X - iZ)^2} + Y_L^2 \right]^{\frac{1}{2}}} \quad (3.1)$$

where $X = Ne^2 / \epsilon_0 m \omega^2 = f_N^2 / f^2$;

$$Y_L = eB \cos \mathbf{q} / m\mathbf{w} = f_H \cos \mathbf{q} / f ;$$

$$Y_T = eB \sin \mathbf{q} / m\mathbf{w} = f_H \sin \mathbf{q} / f ;$$

$$Z = f_v / f ;$$

$$\mathbf{w} = 2\mathbf{p}f ;$$

N is the electron density (el/m³);

f_N is the electron plasma frequency;

f is the radio wave frequency;

e is the electron charge, -1.602×10^{-19} coulomb;

ϵ_0 is the permittivity of free space, 8.854×10^{-12} farads/m;

B is the flux density of the Earth's magnetic field (T);

m is the mass of a electron, 9.107×10^{-31} kg;

\mathbf{q} is the angle between the direction of the wave normal and magnetic field;

f_v is the electron-neutral collision frequency of electrons with heavy particles; and

f_H the electron gyro frequency.

The electron gyro frequency f_H is typically 1.5 MHz; the plasma frequency f_N rarely exceeds 20 MHz; and the collision frequency, f_v , is approximately 10^4 Hz. The first-order phase refractive index can be approximated in an accuracy of better than 1% and it is given by the following formula [Seeber, 1993]:

$$n_p = 1 - (X / 2) \tag{3.2}$$

In the similar way, the group refractive index can be expressed as:

$$n_g = 1 + (X / 2) \quad (3.3)$$

where

$$\frac{X}{2} = \frac{40.3}{f^2} N \quad (3.4)$$

The ionospheric refractive index is the basis for the ionospheric effects on GPS signals. Knowing the refractive index of the ionosphere, it is possible to derive the group delay, the carrier phase advance, and the Doppler shift. It is also possible to calculate the potential effects of Faraday rotation and refraction (or bending) of the radio wave.

3.3 IONOSPHERIC EFFECTS ON GPS

The ionosphere exerts severe influences on the propagation of radio waves which are refracted, reflected and absorbed in various ways according to its dispersive properties. As for GPS applications, the signal delay or advance caused by ionosphere is the major concern because it corrupts the positioning and time transfer results. To get higher accuracy in GPS positioning and navigation, the ionosphere effects must be calibrated.

The ionosphere effects on the GPS measurements are directly reflected in the form of a group delay or a carrier phase advance, which is to be discussed in the following section.

3.3.1 Ionospheric Group Delay and Phase Advance

The group delay of the ionosphere produces pseudorange errors, which can be expressed in units of distance (or in units of time delay) and can be determined by

$$\Delta r = \int (n_g - 1) dl \quad (3.5)$$

From Eq.(3.3), Eq. (3.5) can be expressed by

$$\Delta r = \frac{40.3}{f^2} \int Ndl = \frac{40.3}{f^2} TEC \quad (3.6)$$

The quantity $\int Ndl$ is the Total Electron Content (TEC), in el/m^2 , integrated along the path of l from observer to each GPS satellite. In the same way, the carrier phase advance can be expressed as

$$\Delta \mathbf{f} = \frac{1}{I} \int (n_p - 1) dl = -\frac{40.3}{cf} \int Ndl = -\frac{40.3}{cf} TEC \quad (3.7)$$

The opposite sign in group delay and phase advance indicates the phase velocity is greater than the group velocity. As a consequence of the different velocities, the code pseudoranges are measured longer and the carrier phase pseudoranges are measured shorter than the true geometric range between the satellite and the receiver. The absolute difference, however, is the same in both cases.

3.3.2 Total Electron Content

The Total Electron Content (TEC) is a measure of the total amount of electrons along a arbitrary line of sight. The unit of TEC is a TECU, which is 10^{16} electrons per square metre. In practice, the vertical TEC, which is quantified as the total number of electrons in a vertical column with a cross-sectional area of 1 m^2 , is usually adopted as a characteristic parameter to describe the ionosphere activity [Cannon, 1997]. The value of the vertical TEC varies diurnally, seasonally as well as with an 11-year solar cycle. The diurnal maximum occurs at about 14:00 local time and the minimum usually occurs just before sunrise when the TEC decays due to recombination of electrons and ions. The vertical TEC is also season-related with the maximum usually happening at the Spring Equinox. In addition, the amplitude is different at different geographic locations. The statistics shows that the maximum value usually occurs at 20° latitude at both sides from the geomagnetic equator. Figure 3.3 shows the typical TEC variations within the whole year in middle latitudes.

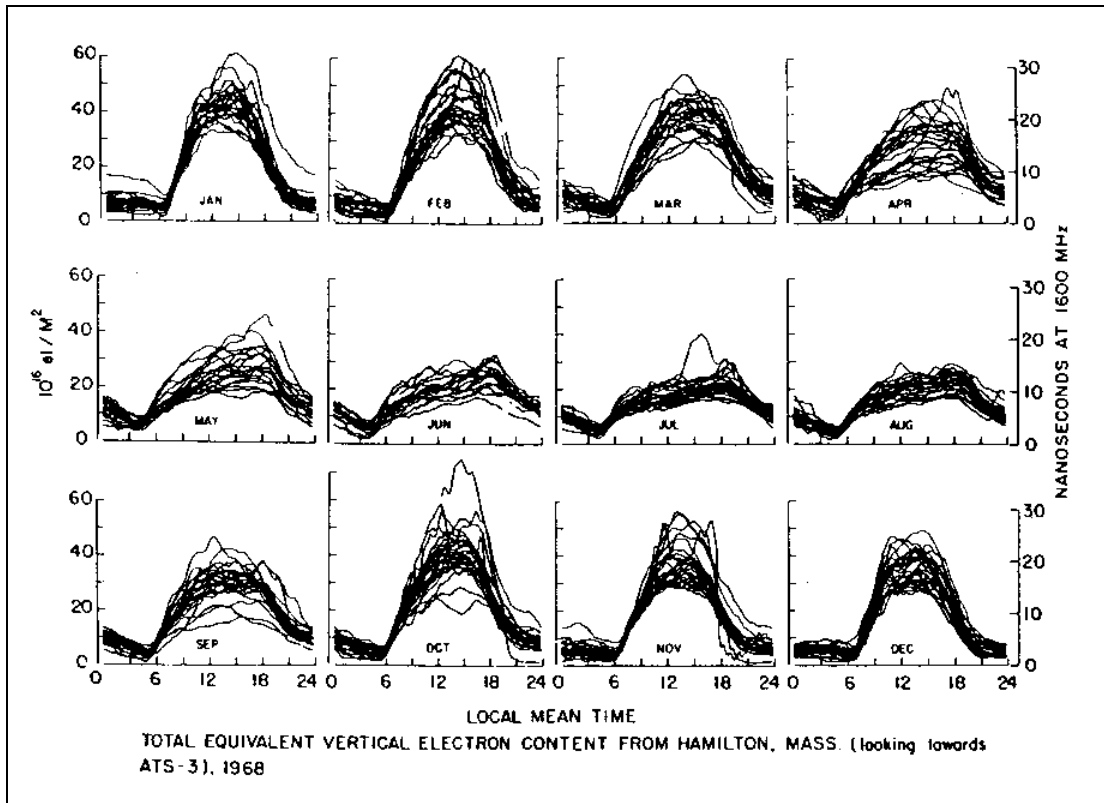


**Figure 3.3 : Day-to-day variations of TEC in middle latitudes.
(in courtesy of Klobuchar, 1978)**

3.3.3 Geomagnetic and Ionospheric Storms

Due to events on the Sun, sometimes the Earth's magnetic field becomes disturbed. The geomagnetic field and the ionosphere are linked in complex ways and a disturbance in the geomagnetic field can often cause a disturbance in the high latitude E region of the ionosphere (Hargreaves, 1992). When geomagnetic storms occur, high velocity particles precipitate into the atmosphere, colliding with neutral atmospheric gases and releasing electrons with emissions of visible light aurora. This kind of storm can occur throughout the solar cycle and are related to coronal mass ejections and coronal holes on the Sun

(Gosling, 1991). They may last for a number of days and, generally, the high latitudes are affected more than the lower latitudes.

Ionospheric storms occurring in mid-latitude or equatorial regions tend to generate large disturbances in ionospheric density distribution, total electron content, and the ionospheric current system [Klobuchar, 1985]. The pattern of the storm effects varies from storm to storm in a complicated way and its dynamic processes that produce these complex variations are not well-understood yet. It should be noted the Global GPS network might be a powerful tool to detect the ionosphere storm and analyze its physical processes.

3.3.4 Ionospheric Scintillation

Small-scale irregularities in the electron content of the ionosphere, with spatial extents from a few metres to a few kilometres, can produce both refraction and diffraction effects on received GPS signals. The refraction changes the direction and speed of propagation of an electromagnetic wave while preserving the phase of the wavefront. The diffraction, on the other hand, results in the wavefront becoming irregular, which, through mutual interference, gives rise to temporal fluctuations in the amplitude and phase of the received signal. Fluctuations due to either effect are called scintillations [Wanninger, 1993].

The region of equatorial scintillations extends 30° on either side of the Earth's magnetic equator with the strongest effects at approximately 10° N and S. There is a clear diurnal variation: scintillations occur between sunset and midnight, and occasionally continue until dawn. In addition, there is a seasonal dependence [Wanninger, 1993]: in the longitude band stretching from the America to India, the effects are strongest between September and March; from April through August, there is only a small chance of significant scintillations in this region. In the Pacific region, however, the situation is reversed. Furthermore, scintillation effects depend on the 11-year solar cycle. Their occurrence increases with an increase in sunspot numbers.

The most severe effects of small-scale ionospheric irregularities are signal fading and signal enhancement, collectively known as amplitude scintillations. As a result of these scintillations, the GPS signal level can drop below a receiver's lock threshold and incur partial data loss and cycle slip. Amplitude scintillations can be monitored by the time series of S/N values provided by the GPS output. Phase scintillations result from sudden changes in ionospheric refraction or from diffraction effects. Because of these scintillations, the phase on both L1 and L2 carriers can change significantly between two consecutive epochs. The resulting rapid frequency change in the received signal associated with phase scintillation effects can cause GPS receiver systems to lose lock. Phase scintillation can be detected using continuous dual-frequency phase data by the time series of Rate Of TEC Index (ROTI). The IGS GPS network has been used successfully by scientists to detect ionospheric scintillations using the indices such as S_4 and S_f [Pi et al., 1999].

3.4 GPS IONOSPHERE MODELLING

Different methods are available to determine the ionosphere delay corrections and then to remove the ionosphere effects from the GPS measurements. In the following, ionosphere correction is discussed with respect to different positioning applications, namely, single frequency Klobuchar model, dual-frequency ionosphere correction, network ionosphere correction.

3.4.1 Klobuchar Model

The Klobuchar ionosphere model uses a sinusoidal curve in fitting to the average diurnal change of the ionosphere. It is adopted by single frequency GPS users. The required ionospheric parameters are broadcast to the GPS users within the fourth subframe of the navigation message. To calculate the ionosphere delay, it also requires knowledge of the user's approximate geodetic latitude, longitude, elevation angle and azimuth to each GPS satellite. Tests have shown that the model can compensate 50-60% of the total ionosphere delay in the middle latitude geographic range [Klobuchar, 1987]. The method can satisfy the general non-precision navigation applications.

3.4.2 Dual-frequency Model

Based on the dispersive property of ionosphere to radio signals, the dual-frequency GPS users can use the pseudorange measurements on L1 and L2 to estimate the ionosphere. From the pseudorange observations, the first-order ionosphere delay on L1 is determined by

$$d_{iono}^{p_1} = (p_2 - p_1) \cdot \frac{f_2^2}{f_1^2 - f_2^2} \quad (3.8)$$

The estimated ionosphere effects thus can be removed from the original pseudorange measurements. However, the noise level is increased in the linear combination. For the carrier phase correction, the ionosphere delay on L1 is determined by

$$d_{iono}^{\Phi_1} = \left\{ \left(\Phi_1 - \frac{f_1}{f_2} \Phi_2 \right) - \left(N_1 - \frac{f_1}{f_2} N_2 \right) \right\} \cdot \frac{f_2^2}{f_2^2 - f_1^2} \quad (3.9)$$

Due to the existence of ambiguities, the absolute ionosphere delay on the carrier phase cannot be determined. However, the differential ionospheric delay over two consecutive epochs can be determined if there is no cycle slip occurrence [Cannon, 1997].

3.4.3 Modelling Over A WADGPS Network

WADGPS is a network approach which consists of multiple sparsely distributed reference stations at a continental scale. Each reference station is equipped with GPS and communication equipment. WADGPS is able to account for the spatial decorrelation of GPS error sources over the large separation distances between the user and the reference sites. It aims to provide metre-level positioning accuracy over a large geographical area and has found increased applications in aviation, marine and agriculture industries. The US Wide Area Augmentation System (WAAS) is a typical WADGPS system. It is expected to provide services in support of enroute through precision approach air navigation in the Continental United States (CONUS) [Enge and Van Dierendonck, 1991].

Since ionospheric delay is the biggest contributor to position errors after SA was turned off, it plays a critical role in WAAS implementation. Although many ionosphere models exist, three of them are most popularly applied, namely grid-model, spherical harmonics, and functional model. To clarify their respective concepts and for the purpose of the later discussion, the three models are described briefly below.

Grid-based model

The grid model was developed by MITRE and the Air Force Phillips Laboratory (AFPL) [El-Arini et al., 1993 & 1994]. It assumes the ionospheric TEC is concentrated within a

thin shell above the Earth. A network of grid points are pre-specified and distributed uniformly on the ionosphere shell and their vertical ionosphere delays are then estimated and broadcast to the users in real-time. At the user point, the ionosphere correction is generated by interpolation using these ionosphere delays at the grid points. Presented in the following is the general steps of ionosphere modelling applied in WAAS and more implementation details can be found in Enge and Van Dierendonck [1995].

Each WAAS reference station measures the ionospheric delays for all visible satellites (the mask angle is normally ≥ 20 degrees) using dual-frequency GPS receivers. The ionosphere delays and the pierce point locations from all reference stations are sent in real time to the master station. The master station collects and combines all the ionospheric data from the distributed reference stations, then estimates the vertical ionospheric delays at each node of an $5^\circ \times 5^\circ$ imaginary fixed grid on the ionospheric sphere. The estimated vertical delays, together with the node latitudes and longitudes, are broadcast via a geo-stationary communication satellite to all the users within the coverage. The user computes the vertical ionosphere delay at the pierce point for each visible satellite through interpolation method using the vertical delays at the four surrounding nodes that surround the pierce point. The slant ionosphere delay is then calculated by the product of the vertical ionosphere delay and a selected mapping function. The details can be referenced to Enge and Van Dierendonck [1995].

Spherical harmonics

Spherical Harmonics (SH) is another option to model the ionosphere in a global or regional area. It can be implemented in terms of the geographic locations of the distributed observation sites. The advantage of using this model lies in the reduced amount of information needed to transmit to the users. The TEC representation using Spherical harmonics is expressed mathematically by [Schaer, 1999]:

$$TEC_v(\mathbf{j}, \mathbf{I}) = \sum_{n=0}^{n_{\max}} \sum_{m=0}^n \tilde{P}_{nm}(\sin \mathbf{j}) (\tilde{C}_{nm} \cos(m\mathbf{I}) + \tilde{S}_{nm} \sin(m\mathbf{I})) \quad (3.10)$$

where

\mathbf{j} is the geomagnetic latitude of the pierce point to the GPS satellite;

\mathbf{I} is the local time (in radian) of the ionospheric pierce point in solar-geomagnetic reference frame;

n_{\max} is the maximum degree of the SH expansion;

$\tilde{P}_{nm} = N_{nm} P_{nm}$ is the normalized associated Legendre function of degree n and order m ;

N_{nm} is the normalization function;

P_{nm} is the classical, un-normalized Legendre function;

$\tilde{C}_{nm}, \tilde{S}_{nm}$ are the unknown SH coefficients of global or regional ionosphere parameters to be estimated.

The ionosphere parameters can be derived using the GPS dual-frequency observations from a distributed reference stations using a least squares method. These parameters can then be used by the users to calculate its ionosphere delay for each visible GPS satellite. The updating interval of the parameters usually depends on the density of the GPS network.

Function-based model

The function-based models describe the vertical ionosphere by a two-dimensional Taylor series expansion:

$$TEC_v(\mathbf{j}, I) = \sum_{n=0}^{n_{\max}} \sum_{m=0}^{m_{\max}} E_{nm} (\mathbf{j} - \mathbf{j}_0)^n (I - I_0)^m \quad (3.11)$$

where

(\mathbf{j}, I) are the solar-geomagnetic latitude and longitude of the ionospheric pierce point;

n_{\max}, m_{\max} are the maximum orders of the two-dimensional Taylor series expansion in latitude and longitude.

E_{nm} are the unknown coefficients of the Taylor series expansion to be estimated;

(\mathbf{j}_0, I_0) are the coordinates of the origin of the expansion.

Similar to the case of spherical harmonics, the unknown coefficients can be estimated by a least square or Kalman filtering method using a batch processing technique. The details of this model can be found in Georgiadou and Kleusberg [1988].

IGS Models

IGS has set up a working group to develop ionosphere models to be used for ionosphere map generation. A number of models have been developed and some are briefly described in the following.

JPL (Jet Propulsion Laboratory) model: The ionosphere vertical TEC is modelled in a solar-geomagnetic reference frame using bi-cubic splines on a spherical grid. A Kalman filter is used to solve simultaneously the L1/L2 instrumental biases and the vertical TEC on the grid points. The parameters are modelled as stochastic process.

UPC (Polytechnical University of Catalonia) model: A stochastic tomographic model is used and the ionosphere is divided into two layers of voxels. The height boundaries are 59-739-1419km.

CODE (Center for Orbit Determination in Europe) model: The TEC is modelled by a spherical harmonics expansion up to degree 12 and order 8 referring to a solar-geomagnetic reference frame. The 12 2-hour sets of ionosphere parameters per day are derived from GPS carrier phase data of the global IGS network.

NRCan (Natural Resource Canada) model: The ionosphere is modelled as a single-layer shell and divided into small cells. The vertical ionosphere TEC in each cell is considered constant during a short time. The ionosphere parameters are estimated in the solar-geomagnetic reference frame.

ESA (European Space Agency): Two dimensional single-layer model as well as a 3D Chapman profile-based model by vertical integration using Gauss-type exponential functions.

3.4.4 Modelling Over A RADGPS Network

With the rapid explosion of GPS networks, there emerges in recent years a concept of Regional Area Differential GPS (RADGPS) which aims at providing decimetre or even centimetre level positioning accuracy [Gao et al., 1997]. With the reference station separation ranging from tens of kilometres to hundreds of kilometres, a RADGPS network provides only a regional area coverage. The ongoing expansion of RADGPS uses around the world has indicated an increased interest within the GPS community. Being complementary to WADGPS and LADGPS (Local Area DGPS), RADGPS is capable of providing centimetre to decimetre accuracy GPS positioning and navigation service. Among many of such networks, the SWEPOS and Norway GPS network in Europe are two typical RADGPS systems in operation.

To achieve the goal of centimetre level positioning, ionosphere modelling in a RADGPS network plays a critical role. Similar to WADGPS, a RADGPS network can also be used to estimate the ionosphere delays above the covered regional area, while the accuracy requirement is much higher. The estimated parameters can in return be used to create ionosphere corrections for the mobile GPS users within that network. The detailed strategy for ionosphere modelling will be discussed in Chapter 4.

CHAPTER 4

CARRIER PHASE BASED IONOSPHERE RECOVERY USING A REGIONAL AREA GPS NETWORK

This chapter describes a new ionosphere recovery method developed for regional area differential GPS positioning and navigation applications. The concept of RADGPS ionosphere recovery is introduced at first, the ionosphere recovery methodology is then discussed in detail in the later part.

4.1 INTRODUCTION

When using RADGPS networks for ionosphere recovery, there are two advantages compared to global-scale or wide area GPS networks. Since a RADGPS network focuses on a relatively small regional area, it can provide a much denser station distribution. As a result, it has much denser GPS signals over the ground network compared to a WADGPS network and, subsequently, a much higher spatial resolution can be achieved in the ionosphere estimation. A high spatial resolution is particularly important especially when large ionosphere gradients and irregularities are present within the covered area. Furthermore, resolving integer ambiguities becomes feasible over relatively shorter baselines in the range of several hundred kilometres. Carrier phase can then be used as the principal observable for ionosphere estimation, which results in much more accurate estimates compared to WADGPS in which the pseudorange is used as the major observable.

A new regional area ionosphere recovery method using a RADGPS network will be described in the rest of the chapter. The discussions are organized as follows. Ionosphere measurements described from carrier phase observations are first examined. A single layer ionosphere grid model is then described. Followed is the detailed discussion of the ionosphere recovery method, which includes the design of a streamlined filter, dynamic and measurement models, sequential processing technique, and system observability with respect to the grid size. Ambiguity resolution will be discussed in Chapter 5. Although the method proposed in this chapter was developed primarily for RADGPS applications, it can also be applied to WADGPS or global-scale applications with only minor modifications if similar distribution density can be assured.

4.2 DERIVATION OF IONOSPHERE MEASUREMENTS

GPS dual-frequency carrier phase measurements are the principal observable used in the regional area ionosphere recovery and their observation equations, according to Eq. (2.2), can be described as

$$\Phi_1 = \mathbf{r} + c(dt - dT) + \mathbf{I}_1 N_1 + d_r + d_{trop} - d_{ion/\Phi_1} + d_{mult/\Phi_1} + \mathbf{e}(\Phi_1) \quad (4.1)$$

$$\Phi_2 = \mathbf{r} + c(dt - dT) + \mathbf{I}_2 N_2 + d_r + d_{trop} - d_{ion/\Phi_2} + d_{mult/\Phi_2} + \mathbf{e}(\Phi_2) \quad (4.2)$$

From Eq. (4.1) and (4.2), we see that the carrier phase measurements are affected by a number of error sources including ionosphere effect. In order to derive the slant ionosphere measurement, we must first resolve the integer ambiguities. Ambiguity

resolution, however, is extremely difficult in a non-differential mode due to the variety of error sources and their significant amplitudes. In order for integer ambiguity resolution to be feasible, we therefore conduct double difference on the carrier phase measurements to remove satellite/receiver dependent errors. The double differenced observation equations can be written as

$$\nabla\Delta\Phi_1 = \nabla\Delta\mathbf{r} + \mathbf{I}_1\nabla\Delta N_1 + \nabla\Delta d_{trop} - k_2\nabla\Delta I + \nabla\Delta d_r + \mathbf{e}(\nabla\Delta\Phi_1) \quad (4.3)$$

$$\nabla\Delta\Phi_2 = \nabla\Delta\mathbf{r} + \mathbf{I}_2\nabla\Delta N_2 + \nabla\Delta d_{trop} - k_1\nabla\Delta I + \nabla\Delta d_r + \mathbf{e}(\nabla\Delta\Phi_2) \quad (4.4)$$

where k_i equals $f_i^2 / (f_1^2 - f_2^2)$;
 f_i is the frequency of GPS signal;
 $\nabla\Delta\Phi_i$ is the measured double difference phase range;
 $\nabla\Delta\mathbf{r}$ is the true geometric double difference range;
 $\nabla\Delta N$ is the double difference phase ambiguity;
 $\nabla\Delta I$ is the double difference ionosphere;
 $\nabla\Delta d_{trop}$ is the double difference troposphere;
 $\nabla\Delta d_r$ is the double difference orbit error;
 $\mathbf{e}(\cdot)$ is the measurement noise including multipath residual.

Eq. (4.3) and (4.4) are the basic observation equations that have been used for the development of ambiguity resolution algorithm to be described in Chapter 5. Once the ambiguities are correctly resolved, the double difference ionosphere measurement can be

derived through a combination of the dual-frequency carrier phase measurements as follows

$$\nabla\Delta\hat{I} = \nabla\Delta\Phi_1 - \nabla\Delta\Phi_2 - (I_1\nabla\Delta N_1 - I_2\nabla\Delta N_2) \quad (4.5)$$

This is the ionosphere measurement that has been used for regional ionosphere recovery to be discussed in the later sections.

4.3 A SINGLE LAYER IONOSPHERE GRID MODEL

The ionosphere is a region of ionized plasma that extends from roughly 50 km to 2000km above the surface of the Earth. The ionization process is mainly imposed by the absorption of solar ultraviolet radiation and x-ray radiation thus leading to the diurnal variation of the ionosphere. The behavior of the ionosphere is also controlled by the Earth's magnetic field, due to the impacts of the latter on the movements of the electrons. The existence of a significant number of free electrons in the ionosphere results in the signal delay or advance when the radio signal penetrates the layer. Moreover, the ionosphere can be divided into several layers in altitude according to the different electron densities, with a peak value at about 350km in altitude. This property makes it possible to approximate the ionosphere by a simplified model of one thin shell when considering the delay effects on GPS signal [Gao et al., 1994].

In this research, we describe ionosphere within a solar-geomagnetic reference system instead of an Earth-fixed reference system. A solar-geomagnetic coordinate system is advantageous in several aspects. Firstly, ionosphere is much more stable in this system than in the Earth-fixed system and subsequently, it helps find out an appropriate stochastic process to describe the behavior of the ionosphere. Secondly, for the thin shell ionosphere model, the ionosphere pierce points are more vastly distributed in solar-geomagnetic system, although with the same quantity of observations, versus in Earth-fixed system. Therefore, with the same fixed grid interval, more grid points thus a larger area of ionosphere can be recovered in the vertical TEC estimation when ionosphere is modelled in the solar-geomagnetic system.

The implementation of the single-layer model requires computation of the intersection of the line-of-sight between the GPS receiver and the observed satellite with the ionospheric shell at 350 km altitude as shown in Figure 4.1. The geographic location of the pierce point, calculated from the known geographic location of the receiver and the satellite coordinates, is transformed to geomagnetic coordinates. The geomagnetic longitude is further transformed to the local hour angle which is defined as

$$\mathbf{f}_{Local} = T_{UTC} + \mathbf{f}_m \quad (4.6)$$

where T_{UTC} is the UTC time of the observation epoch at the receiver station and \mathbf{f}_m is the corresponding geomagnetic longitude of the intersection point at the ionospheric shell.

Different local hour angles correspond to different TEC values assuming the ionospheric structures are approximately stationary with respect to the solar-geomagnetic system.

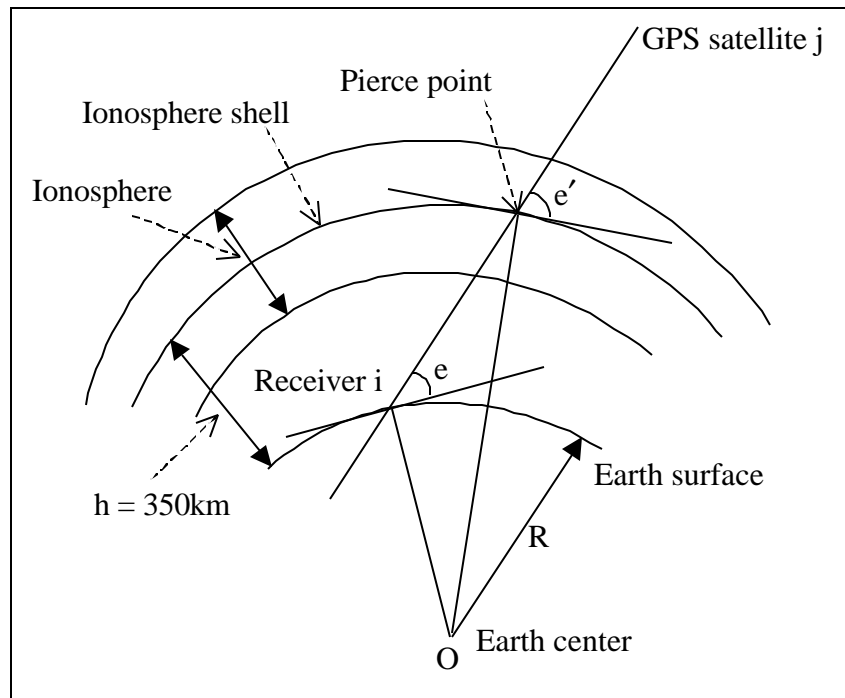


Figure 4. 1: Slant ionosphere path illustration.

An alternative to the grid model is the spherical harmonics model. Since it uses a smoothing or fitting technique, it might not be adequate for regional or local area ionosphere recovery especially when the ionosphere has large gradients requiring high spatial resolution.

For the research in this thesis, a single shell grid model with respect to the solar-geomagnetic reference frame has been developed for regional area ionosphere modelling. The implementation of such a model in ionosphere recovery will be discussed in Section 4.4.

4.4 A STREAMLINED KALMAN FILTER

4.4.1 The Concept

For global-scale ionosphere recovery, the vertical TEC values at all the grid points on the shell can be included as unknowns within a single estimator. They remain in the Kalman filter during the entire estimation period and are continuously updated as time proceeds. For ionosphere recovery using a non-global scale network such as RADGPS networks, a different strategy must be employed simply because only part of the global ionosphere can be seen by the ground GPS stations at any given time. As a result, only those grid points locally visible by the network at that time need to be updated using the newly available measurements from the network. Further, since the GPS network is rotating with the Earth, the grid points visible by the local network are different at different times. For a specific grid point, for instance, it will start to be visible by the network at some time and will then be out of sight after a period of time as the Earth rotates.

Our estimation strategy has then been to put an imaginary fixed-size window on the ionosphere shell, as shown in Figure 4.2, to enclose all visible grid points at a given time as state variables in our estimator. As a result, only those grid points will be updated at that time epoch. The window will move as the Earth rotates (with a speed of about 15 degrees per hour) to remain above the ground network. The geomagnetic local hour angles of the pierce points for all the satellites will increase in an approximate linear

pattern as the Earth rotates. Shown in Figure 4.3 are the geomagnetic local hour angles of the pierce points for 3 satellites observed by a network of ten ground stations (see Figure 6.3). It indicates that the geomagnetic local hour angle change of the pierce points is not significantly affected by the satellite movements, but controlled dominantly by the rotation of the Earth. After the Earth completes one cycle of rotation, the trace made by the window will form a complete geomagnetic latitude band on the ionosphere shell. The window size is dependent on the network geographic range as well as the satellite cutoff angle.

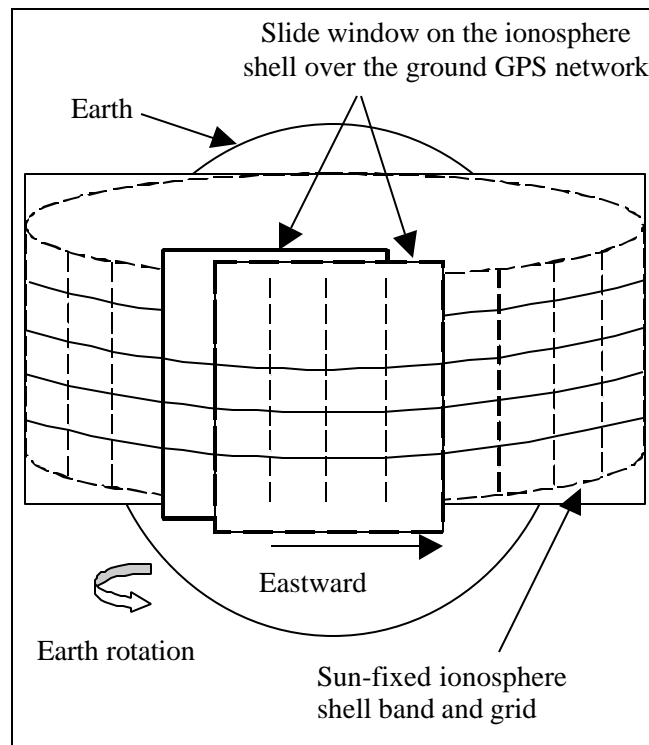


Figure 4. 2: A regional area ionosphere grid model.

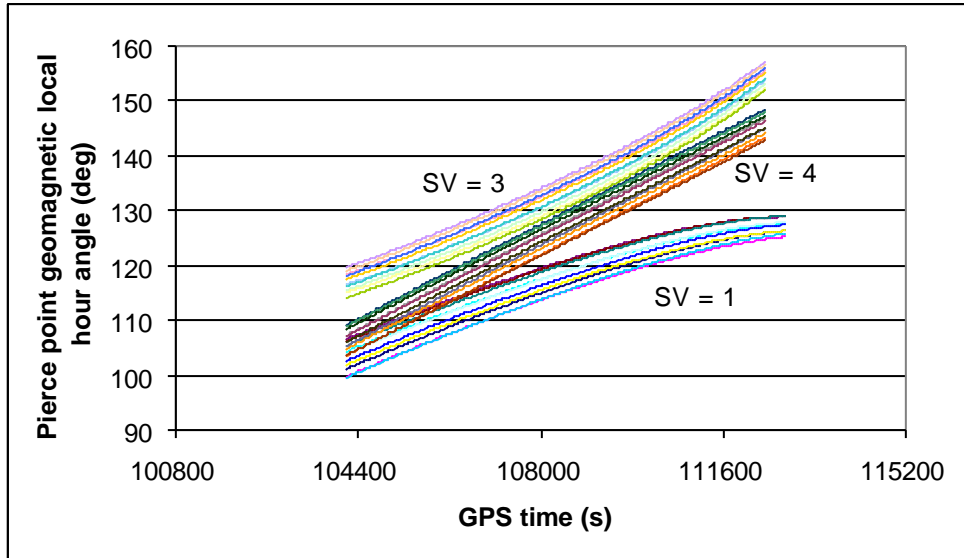


Figure 4. 3: Geomagnetic local hour angle of the pierce points for 3 GPS satellites.

Based on the above discussion, our Kalman filter is designed to include only the vertical TEC parameters of those grid points within the window at a given time. Therefore, the filter size is much smaller. In the time domain, if a grid point moves out of the window, its vertical TEC parameter will be eliminated from the state vector. At the same time, the vertical TEC parameters at the grid points that are moving into the window will be added into the state vector. Therefore, the Kalman filter is a streamlined estimator as shown in Figure 4.4.

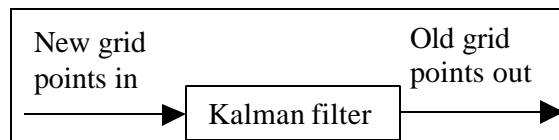


Figure 4. 4: Streamlined Kalman filter.

Let the updated state vector and the corresponding covariance at the (k-1)-th epoch be expressed mathematically as

$$X_{k-1}^{(+)} = [x_1^{(+)}, \dots, x_m^{(+)}, x_{m+1}^{(+)}, \dots, x_n^{(+)}]_{k-1} \quad (4.7)$$

$$P_{k-1}^{(+)} = \begin{bmatrix} p_{1,1}^{(+)} & \cdots & p_{1,m}^{(+)} & p_{1,m+1}^{(+)} & \cdots & p_{1,n}^{(+)} \\ \vdots & \ddots & \vdots & \vdots & \vdots & \vdots \\ p_{m,1}^{(+)} & \cdots & p_{m,m}^{(+)} & p_{m,m+1}^{(+)} & \cdots & p_{m,n}^{(+)} \\ p_{m+1,1}^{(+)} & \cdots & p_{m+1,m}^{(+)} & p_{m+1,m+1}^{(+)} & \cdots & p_{m+1,n}^{(+)} \\ \vdots & \vdots & \vdots & \vdots & \ddots & \vdots \\ p_{n,1}^{(+)} & \cdots & p_{n,m}^{(+)} & p_{n,m+1}^{(+)} & \cdots & p_{n,n}^{(+)} \end{bmatrix}_{k-1} \quad (4.8)$$

where n is the total number of the grid points or states in the Kalman filter;

x_i is the state of the vertical TEC at the i-th grid point;

$p_{i,j}$ is the covariance between the states of the vertical TEC at the i-th and j-th grid points.

Suppose that the first m grid points have moved out of the slide window and at the same time m new grid points have just moved into the window at the k-th epoch. The prediction state vector and its covariance matrix at the k-th epoch have the forms of

$$X_k^{(-)} = [x_{m+1}^{(-)}, \dots, x_n^{(-)}, x_{n+1}^{(-)}, \dots, x_{n+m}^{(-)}]_k \quad (4.9)$$

$$P_k^{(-)} = \begin{bmatrix} p_{m+1,m+1}^{(-)} & \cdots & p_{m+1,n}^{(-)} & 0 & 0 & 0 \\ \vdots & \ddots & \vdots & 0 & 0 & 0 \\ p_{n,m+1}^{(-)} & \cdots & p_{n,n}^{(-)} & 0 & 0 & 0 \\ 0 & 0 & 0 & p_{n+1,n+1}^{(-)} & 0 & 0 \\ 0 & 0 & 0 & 0 & \ddots & 0 \\ 0 & 0 & 0 & 0 & 0 & p_{n+m,n+m}^{(-)} \end{bmatrix}_k \quad (4.10)$$

From Eq. (4.9) and (4.10), the last $n - m$ grid points at the $(k-1)$ -th epoch still remain in the Kalman filter and the m new grid points have been added into the filter. The initial variance of the vertical TEC for the new grid points is usually set to a large value while the covariance values between the new states and the old states are initially set to zero due to the lack of priori correlation information. Once the prediction is completed, the updating is performed in the same manner as the previous epochs by the sequential processing method which will be discussed later.

4.4.2 Dynamic Model

At any given epoch and considering all data prior to it, only the vertical TEC of those grid vertices that fall within the slide window will be updated using the Kalman filtering technique. Any grid vertex in the geomagnetic latitude band during a complete Earth rotation cycle will have opportunities to be updated within a certain period of time in the whole day due to the regional scale of the network. The average updating time period depends on the size of the network in longitude and the cutoff angle. At different grid vertices, the updating time period could be different. Typically, it will last several hours during which the vertical TEC at the grid vertices can be modelled as a stochastic

process. For this thesis, a random walk process is adopted, which can describe very well the behavior of the vertical ionosphere TEC at the grid points over time in solar-geomagnetic reference system under normal ionosphere conditions. The random walk model is described as follows

$$(I_v)_{k+1} = (I_v)_k + w_k \quad (4.11)$$

where w_k is the un-modelled ionosphere change during one update interval. It is considered as a white noise with variance of Q_k . As we know, the ionosphere shell is stable with respect to the reference frame when it is modelled in the solar-geomagnetic system, some typical empirical values of Q_k can be used when modelling the ionosphere. A variation of several TEC units per hour is adequate for the dynamic modelling. The results, however, have shown that the vertical TEC estimates are insensitive to Q_k . In some regions when ionosphere disturbance is likely to occur, an adaptive model can be chosen to adjust the model in response to the fast changing ionosphere [Skone, 1998].

4.4.3 Measurement Model

The double difference carrier phase derived ionosphere measurements in Eq. (4.5) are the primary observable in the ionosphere recovery. As shown in Figure 4.5, the double difference ionosphere measurement is a combination of the undifferenced slant ionosphere at four pierce points. Each undifferenced slant ionosphere can be mapped to the vertical direction at the associate pierce point by the following mapping function:

$$sf(e) = \{1 - [\cos(e)/(1 + h/R)]^2\}^{\frac{1}{2}} \quad (4.12)$$

where e is the satellite elevation angle;

R is the Earth radius;

h is the assumed height of maximum electron density (350 km for our case).

The mapping function assumes a constant ionospheric centroid height of the single shell, which is an approximation over the regional network. In the case of large spatial gradients and small elevation angle (i.e. $<15^\circ$), the assumptions may cause significant errors. Detailed discussion can be found in Skone [1998].

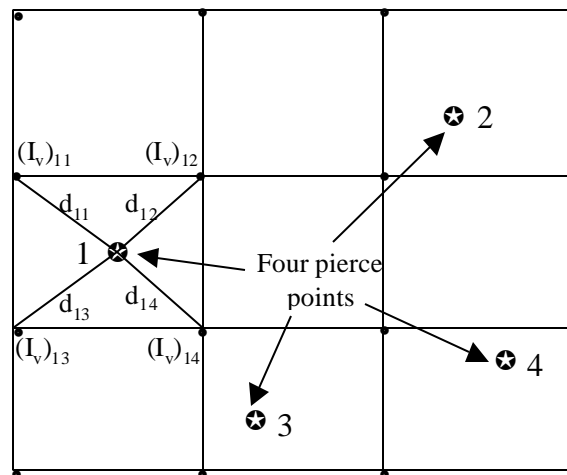


Figure 4. 5: A function model of double difference ionosphere measurement with the vertical TEC of the surrounding grid points.

In order to recover the vertical TEC at the grid points, the mapped vertical TEC measurement at each pierce point needs to link to the vertical TEC at the surrounding

four grid points. A weighting function is often used for this purpose. In this thesis, the following model has been developed to establish the functional relationship between the double difference ionosphere measurements and the vertical ionosphere over the surrounding grid points:

$$\nabla\Delta I = sf_1 \cdot \sum_{j=1}^4 (I_v)_{1j} \cdot w_{1j} - sf_2 \cdot \sum_{j=1}^4 (I_v)_{2j} \cdot w_{2j} - sf_3 \cdot \sum_{j=1}^4 (I_v)_{3j} \cdot w_{3j} + sf_4 \cdot \sum_{j=1}^4 (I_v)_{4j} \cdot w_{4j} \quad (4.13)$$

where sf_i is the slant factor;

w_{ij} is the weighting function;

$(I_v)_{ij}$ is the vertical ionosphere TEC at the associate grid points.

Once a double difference ionosphere measurement is available from the network, a sequential Kalman filtering updating will then be conducted as described in the next subsection.

There are several weighting functions available but results in El-Arini et al. [1994] have indicated that there is little difference in accuracy between different functions. We choose the inverse distance weighting function integrated with the Klobuchar model, and it is expressed as

$$w_{ij} = \left(\frac{\mathbf{t}_i}{\mathbf{t}_j} \right) \frac{\frac{1}{d_{ij}}}{\sum_{k=1}^4 \frac{1}{d_{ik}}} \quad (4.14)$$

where \mathbf{t}_i is the predicted vertical ionospheric delay at the i -th pierce point as estimated by the Klobuchar ionospheric model, \mathbf{t}_j is the predicted vertical ionospheric delay at the j -th grid point as estimated by the same ionospheric model.

Eq. (4.13) is not only used as the measurement model in ionosphere recovery, but also used to estimate the double difference ionosphere at the user receiver where the double difference ionosphere is recovered as an external source for consistency examination.

4.4.4 Sequential Filtering

For a regional area GPS network, it is common that most reference stations can have 5-9 commonly visible satellites at any time. For such a configuration, there will be dozens of double difference ionosphere measurements available at each epoch to update the vertical TEC states for all the visible grid points. If the Kalman filter implements the update at each epoch by a single step for all measurements, the calculation efficiency will be much degraded due to the overload work of large matrix operations. Therefore, sequential processing is preferred in this case. The state updating in our filter is conducted for each measurement at a time. It has also reduced the complexity of the filter design. The Kalman filtering models are described as follows

State model:

$$X_k = \Phi_{k,k-1}X_{k-1} + G_{k-1}W_{k-1}$$

Measurement model:

$$Y_k = H_k X_k + V_k$$

Prediction:

$$X_k^{(-)} = \Phi_{k,k-1}X_{k-1}^{(+)} \quad (4.15a)$$

$$P_k^{(-)} = \Phi_{k,k-1}P_{k-1}^{(+)}\Phi_{k,k-1}^T + G_{k-1}Q_{k-1}G_{k-1}^T \quad (4.15b)$$

Update:

$$X_k^{(+)} = X_k^{(-)} + K_k(Y_k - H_k X_k^{(-)}) \quad (4.16a)$$

$$K_k = P_k^{(-)}H_k^T[H_kP_k^{(-)}H_k^T + R_k]^{-1} \quad (4.16b)$$

$$P_k^{(+)} = (I - K_kH_k)P_k^{(-)} \quad (4.16c)$$

where

X_k is the state vector;

$\Phi_{k,k-1}$ is the transition matrix;

G_{k-1} is the matrix associated to the system noise;

W_k is the system noise, and

$$E[W_k] = 0; \quad E[W_k W_l^T] = \begin{cases} Q_k, & k = l \\ 0, & k \neq l \end{cases};$$

V_k is the measurement noise, and

$$E[V_k] = 0; E[V_k V_l^T] = \begin{cases} R_k, & k = l \\ 0, & k \neq l \end{cases};$$

H_k is the design matrix;

Y_k is the measurement vector;

K_k is the gain matrix;

X_k^-, P_k^- is the predicted state vector and covariance matrix at k-th epoch;

X_k^+, P_k^+ is the updated state vector and covariance at k-th epoch.

In sequential processing for our case, the transition matrix $\Phi_{k,k-1}$ and design matrix H_k in the above dynamic and measurement models are unit matrix and vector, respectively.

Since the absolute vertical TEC is estimated using differenced carrier phase measurements, the geometry may be degraded compared to the undifferenced case. If the lines-of-sight for different GPS stations with respect to the same satellite are too close, the resulting TEC estimates are likely to be unstable. This situation will occur if the GPS network is small and the reference station separation is too short. As for a GPS network which constitutes a coverage of several hundred kilometres, the geometry configuration is distinguishable between the stations. Figure 4.6 demonstrates the maximum zenith difference with respect to the same satellite may reach over 6 degrees among all the ten stations in the SWEPOS network (shown in Figure 6.3). Moreover, the dense network has

a lot of redundant measurements and the geometry is continuously changing as the satellites are orbiting around the Earth. This allows for the extraction of the absolute vertical TEC values from the double difference ionosphere measurements even under relatively weak geometry configuration.

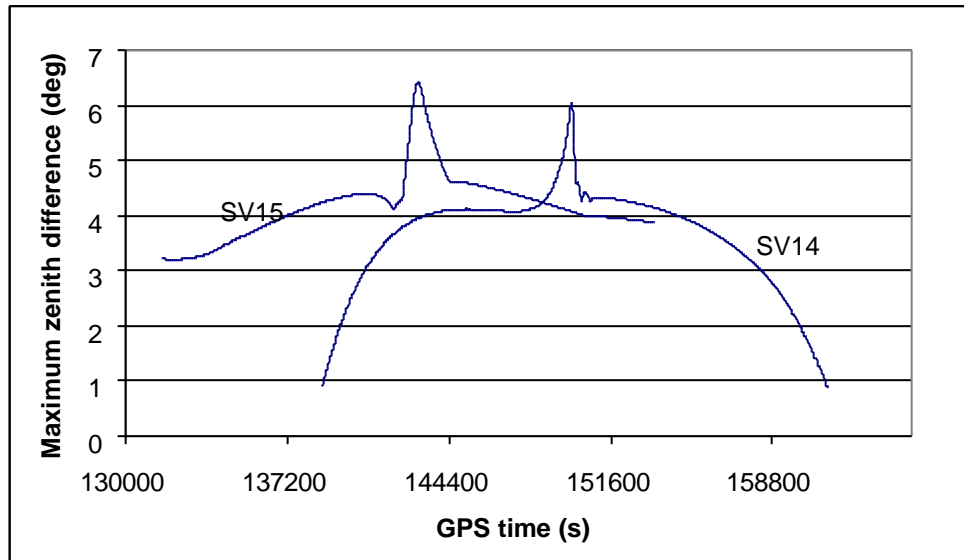


Figure 4. 6: Typical maximum zenith difference.

4.5 GRID SIZE AND OBSERVABILITY

Since a regional GPS network is usually a dense network, it allows for the selection of a small grid size. However, the size selection must account for two factors. Preferably, a high spatial resolution is required for a regional network to deal with rapid ionosphere variation over the area. High spatial resolution requires small grid size. On the other hand, to guarantee the system's observability, the grid size, however, can not be too small because too small a grid size may lead the vertical TEC at some grid points to be

unobservable. A grid size of $1.5^{\circ} \times 1.5^{\circ}$ is appropriate for a typical regional area GPS network considering the fact that the Earth rotates at a speed of about 15 degrees per hour with respect to the solar-geomagnetic frame. It takes about six minutes for a pierce point of a satellite to move out of a grid cell. With a sample rate of 30 seconds in data acquisition, there will be about 12 pierce points that will fall into that cell during that period of time. Figure 4.7 shows the pierce point tracks of one satellite observed by ten ground stations (shown in Figure 6.3). It shows clearly the pierce point movement over the ionosphere shell as the satellite moves continuously. With all the visible satellites from the whole network, there would be enough measurements inside the cell to precisely estimate the vertical TEC at the surrounding four grid points.

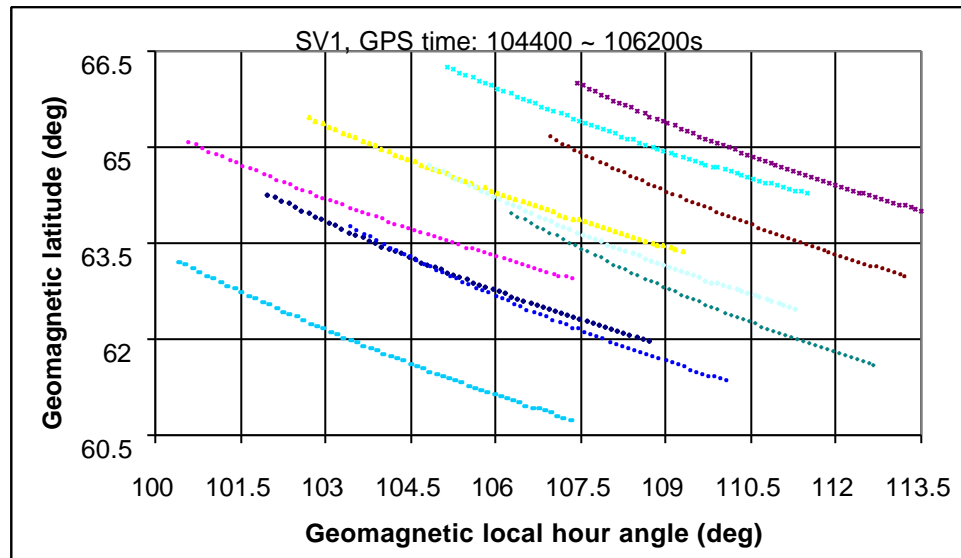


Figure 4.7: The tracks of pierce points for one visible satellite.

Shown in Figure 4.8 are all the pierce points lying within a certain range of ionosphere shell observed by ten ground GPS stations (shown in Figure 6.3). Although some pierce

points observed by different stations lie within the same cells, the arriving times of those pierce points are different. It indicates that the vertical TEC at grid points can be estimated accurately because there are sufficient pierce points lying within their surrounding cells. It also indicates that a dense regional area GPS network will have better performance over the WAAS or global-scale GPS networks whose pierce points will be much more sparsely distributed on some of the ionosphere shell.

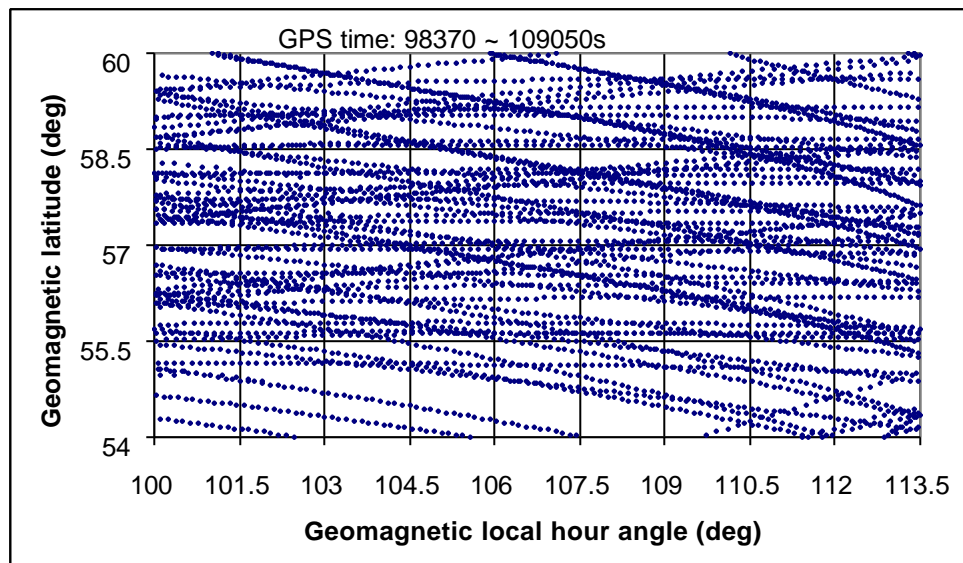


Figure 4. 8: The pierce points for all visible satellites in the solar-geomagnetic reference frame.

CHAPTER 5

REGIONAL AREA GPS NETWORK AMBIGUITY RESOLUTION

This chapter will discuss the carrier phase ambiguity resolution for regional GPS networks. The error mitigation techniques such as troposphere modelling and precise orbit utilization will first be presented. The ambiguity resolution method is then discussed including ambiguity search space definition, ambiguity discrimination and misclosure constraint.

5.1 GPS ERROR REDUCTION

As indicated in Eq. (4.5), carrier phase ambiguities on both frequencies must be first resolved before double difference ionosphere measurements can be derived. From Eq. (4.3) and (4.4), it indicates that the residual troposphere and orbital effects must be removed or reduced to a negligible level with respect to the wavelength of the integer ambiguities in order to facilitate the ambiguity resolution. Multipath error can usually be mostly eliminated by the use of a choke ring above the antenna and the residual multipath errors in the double differenced carrier phase measurements can then be considered at a negligible level. In the following, we will focus on troposphere and orbital error reductions.

5.1.1 Troposphere Error

There are many troposphere models available, among them Saastamoinen-Niell model is preferred as to the estimation of the zenith dry and wet components of the troposphere corrections [Hay and Wong, 2000]. We choose this model for troposphere error reduction and use standard parameters of pressure, temperature and humidity. Results indicated that the performance of the combined Saastamoinen and Niell model is better than other proposed models. The Saastamoinen troposphere model for the dry and wet components are described as follows:

The dry zenith delay:

$$d_d^z = 10^{-6} K_1 R_d P_s / g_m \quad (5.1)$$

where K_1 is a refractivity coefficient, R_d is the gas constant for dry air, P_s is the site pressure, and g_m is the local gravity.

The wet zenith delay:

$$d_w^z = 0.002277(1255 / T + 0.05)e \quad (5.2)$$

where T is surface temperature and e is the surface water vapor pressure.

The Niell mapping function is expressed as [Niell et al., 1996]:

$$m(\mathbf{e}) = \frac{1 + \frac{a}{1 + \frac{b}{1 + c}}}{\sin \mathbf{e} + \frac{a}{\sin \mathbf{e} + \frac{b}{\sin \mathbf{e} + c}}} \quad (5.3)$$

where ε is the elevation angle, and a , b , and c are empirically determined coefficients. The coefficients for dry part depend on the latitude and the height at the observing site and on the day of the year, while the coefficients for wet part depend only on the site latitude.

Figure 5.1 shows the typical double difference troposphere delays before and after applying the troposphere correction. Double difference ionosphere from carrier phase and pseudorange are also shown in the figure. To be observed clearly, the double difference troposphere residual is amplified in Figure 5.2. It's clear to see the troposphere effects are significantly eliminated after the use of the troposphere reduction model.

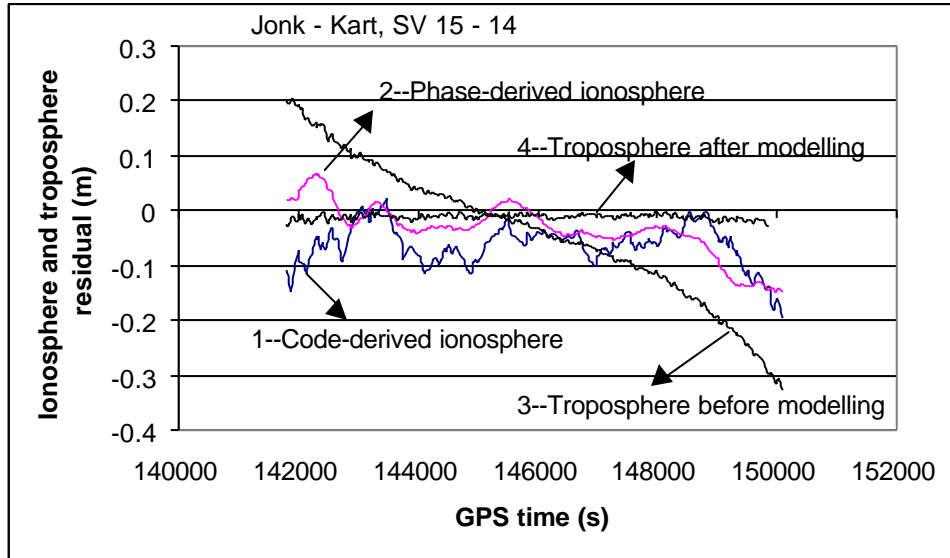


Figure 5. 1: Double difference ionosphere delay and troposphere residual.

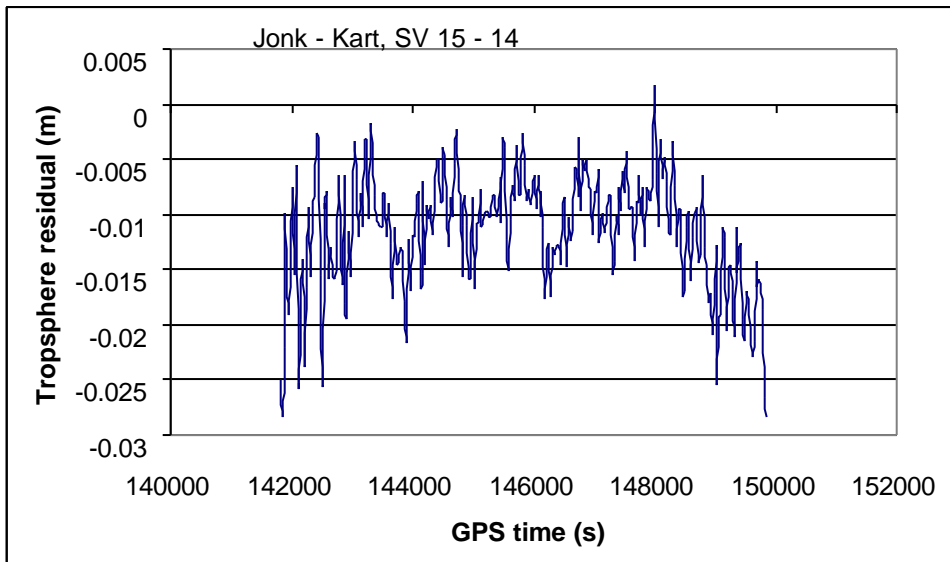


Figure 5. 2: Double difference troposphere residual after modelling.

5.1.2 Orbital Error

The broadcast ephemeris is not accurate enough to totally remove the orbit error even in double difference observations. Experiments have shown that the residual orbital error will make it difficult to fix the ambiguity. Precise orbit is therefore required for long baseline ambiguity resolution. Currently the most accurate orbital information is provided by the IGS, with the accuracy of 5 cm in a delay of one week. The IGS precise orbit can be accessed free of charge for all users through the website (<http://igsb.jpl.nasa.gov/>). It is expected that precise orbit will be available in real-time or near real-time in the future.

The precise orbits consist of satellite positions and clock corrections with a data rate of 15 minutes in SP3 format. The position and velocity vectors at any intermediate epoch between the given epochs can be obtained, with a compatible accuracy, by Lagrange interpolation based on a set of polynomial base functions. Studies in Remondi [1989] concluded that for GPS satellites a 30-minute epoch interval and a 9th-order interpolator suffices for an accuracy of about 10^{-8} . The principle of Lagrange interpolation has been described in Moritz [1977].

Assume functional values $f(t_j)$ are given at epochs t_j ($j = 0, \dots, n$). The corresponding n -order base function $l_j(t)$ for any arbitrary epoch t can be expressed as

$$l_j(t) = \frac{(t-t_0)(t-t_1)\cdots(t-t_{j-1})(t-t_{j+1})\cdots(t-t_n)}{(t_j-t_0)(t_j-t_1)\cdots(t_j-t_{j-1})(t_j-t_{j+1})\cdots(t_j-t_n)} \quad (5.4)$$

The interpolated functional value at epoch t can then be expressed as

$$f(t) = \sum_{j=0}^n f(t_j)l_j(t) \quad (5.5)$$

Figure 5.3 shows the difference between the station-satellite geometric ranges calculated respectively using the precise orbit and the broadcast ephemeris. It shows that the difference can reach more than one hundred metres. Even after double difference, the difference between the calculated geometric ranges can still be at the level of several metres as indicated in Figure 5.4. This indicates the orbit errors will largely affect the ambiguity resolution if the broadcast ephemeris is used. Precise orbit therefore must be employed in this case for reliable ambiguity resolution.

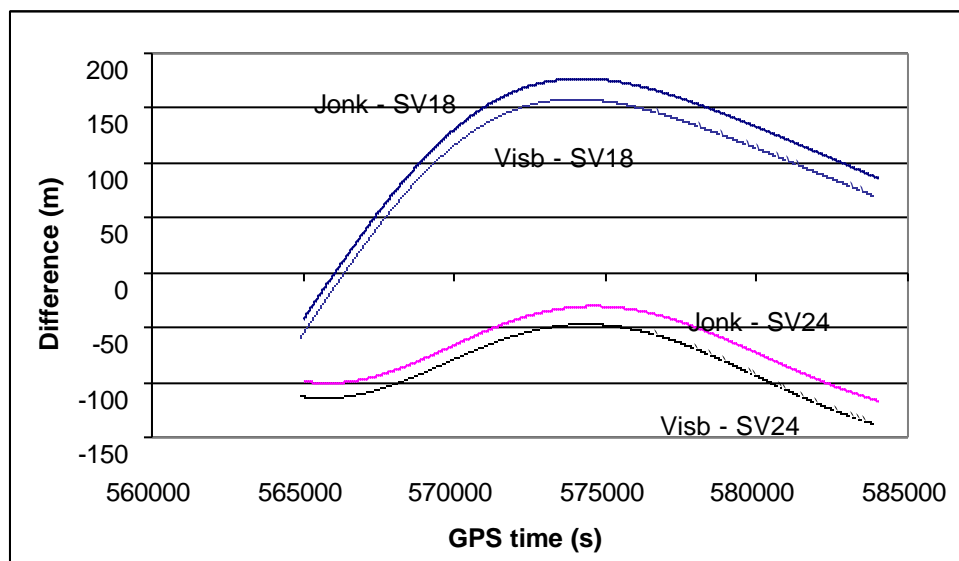


Figure 5. 3: Geometric range difference between precise and broadcast ephemeris.

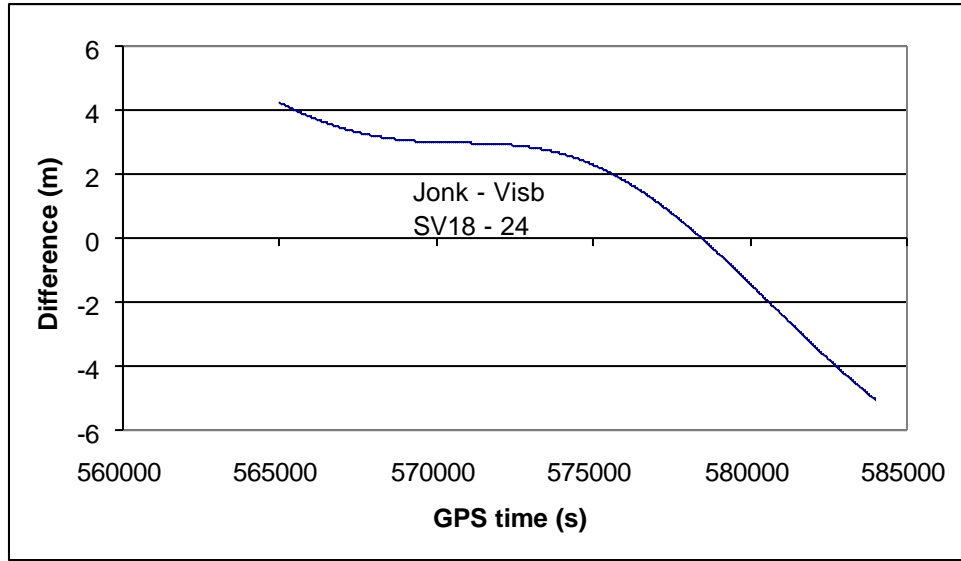


Figure 5. 4: Difference between the double difference geometric ranges using precise and broadcast ephemeris.

5.1.3 Reduced Phase Observable Equations

With troposphere, satellite orbit and multipath errors eliminated from Eq. (4.3) and (4.4) or significantly smaller than the wavelength of the integer ambiguities, the observation equations Eq. (4.3) and (4.4) can be reduced to

$$\nabla\Delta\Phi_1 = \nabla\Delta\mathbf{r} + \mathbf{I}_1\nabla\Delta N_1 - k_2\nabla\Delta I + \mathbf{e}(\nabla\Delta\Phi_1) \quad (5.6)$$

$$\nabla\Delta\Phi_2 = \nabla\Delta\mathbf{r} + \mathbf{I}_2\nabla\Delta N_2 - k_1\nabla\Delta I + \mathbf{e}(\nabla\Delta\Phi_2) \quad (5.7)$$

which become the carrier phase equations used in ambiguity resolution.

5.2 DEVELOPMENT OF AN AMBIGUITY RESOLUTION ALGORITHM FOR REGIONAL AREA GPS NETWORKS

Two options may exist as to regional GPS network ambiguity resolution. One is called the combined approach, in which both vertical TEC and integer ambiguity parameters are estimated simultaneously. The method, however, requires the design of a large Kalman filter and will be computationally less cost-effective. An alternative to the above is to divide the estimation process into two sub-procedures: first resolve the ambiguities and then derive ionosphere measurements needed for ionosphere recovery. In this way, the complexity of the Kalman filter will be significantly reduced and in turn the computation becomes more efficient. The second approach is also considered more feasible for real-time applications and is adopted in this thesis.

5.2.1 Ambiguity Search Space

To develop a fast and reliable ambiguity search method for a regional GPS network, an efficient search space should be first defined to ensure that the search range contains the true ambiguities while the search range is as small as possible. The following ionosphere combination and ionosphere-free combination measurements have been used to determine the initial L1 and L2 ambiguities:

- Ionosphere combination:

$$\nabla\Delta\Phi_{ion} = \nabla\Delta\Phi_1 - \nabla\Delta\Phi_2 = \frac{I_1}{60}\nabla\Delta N_{ion} + \nabla\Delta I + \mathbf{e}(\nabla\Delta\Phi_{ion}) \quad (5.8)$$

- Ionosphere-free combination:

$$\begin{aligned}\nabla\Delta\Phi_{IF} &= \frac{77f_1}{77f_1 - 60f_2} \nabla\Delta\Phi_1 - \frac{60f_2}{77f_1 - 60f_2} \nabla\Delta\Phi_2 \\ &= \nabla\Delta\mathbf{r} + \frac{c}{77f_1 - 60f_2} \nabla\Delta N_{77,-60} + \mathbf{e}(\nabla\Delta\Phi_{IF})\end{aligned}\quad (5.9)$$

where c is the speed of light; and

$$\nabla\Delta N_{ion} = 60\nabla\Delta N_1 - 77\nabla\Delta N_2$$

$$\nabla\Delta N_{77,-60} = 77\nabla\Delta N_1 - 60\nabla\Delta N_2$$

From Eq. (5.8) and (5.9), the initial ambiguities $\nabla\Delta N_{ion}^0$ and $\nabla\Delta N_{IF}^0$ can be determined by

$$N_{ion}^0 = \frac{60}{\mathbf{I}_1} \cdot \nabla\Delta\Phi_{ion} \quad (5.10)$$

$$N_{IF}^0 = \frac{77f_1 - 60f_2}{c} \cdot (\nabla\Delta\Phi_{IF} - \nabla\Delta\mathbf{r}) \quad (5.11)$$

Considering possible residual errors in troposphere modelling, precise orbit and multipath, we define confidence intervals for the initial ambiguities $\nabla\Delta N_{ion}^0$ and $\nabla\Delta N_{IF}^0$, i.e.

$$\left| \nabla\Delta N_{ion} - \nabla\Delta N_{ion}^0 \right| < \mathbf{g}_{ion} \quad (5.12)$$

$$\left| \nabla\Delta N_{IF} - \nabla\Delta N_{IF}^0 \right| < \mathbf{g}_{IF} \quad (5.13)$$

We can then define the search range for $\nabla\Delta N_1$ and $\nabla\Delta N_2$:

$$\begin{aligned} & \frac{(77\nabla\Delta N_{IF}^0 - 60\nabla\Delta N_{ion}^0) - (60\mathbf{g}_{ion} + 77\mathbf{g}_{IF})}{2329} \\ & < \nabla\Delta N_1 < \frac{(77\nabla\Delta N_{IF}^0 - 60\nabla\Delta N_{ion}^0) + (60\mathbf{g}_{ion} + 77\mathbf{g}_{IF})}{2329} \end{aligned} \quad (5.14)$$

$$\begin{aligned} & \frac{(60\nabla\Delta N_{IF}^0 - 77\nabla\Delta N_{ion}^0) - (77\mathbf{g}_{ion} + 60\mathbf{g}_{IF})}{2329} \\ & < \nabla\Delta N_2 < \frac{(60\nabla\Delta N_{IF}^0 - 77\nabla\Delta N_{ion}^0) + (77\mathbf{g}_{ion} + 60\mathbf{g}_{IF})}{2329} \end{aligned} \quad (5.15)$$

The confidence intervals \mathbf{g}_{ion} and \mathbf{g}_{IF} in Eq. (5.12) and (5.13) depend on the residual error of the ionosphere combination and ionosphere-free combination measurements:

$$\mathbf{g}_{ion} = c_{ion} \cdot \frac{60}{I_1} \cdot \mathbf{s}_{\nabla\Delta\Phi_{ion}} \quad (5.16)$$

$$\mathbf{g}_{IF} = c_{IF} \cdot \frac{77f_1 - 60f_2}{c} \cdot \mathbf{s}_{\nabla\Delta\Phi_{IF}} \quad (5.17)$$

where c_{ion} and c_{IF} are two predefined integers. It is clear that the greater c_{ion} and c_{IF} the larger the corresponding search ranges. In practice, c_{ion} and c_{IF} can be set to 3. In this case, if we let $\mathbf{s}_{\nabla\Delta\Phi_{ion}} = 1$ and $\mathbf{s}_{\nabla\Delta\Phi_{IF}} = 1$, for example, we have

$$\mathbf{g}_{ion} \approx 946; \mathbf{g}_{IF} \approx 477$$

From Eq. (5.14) and (5.15), the search ranges for $\nabla\Delta N_1$ and $\nabla\Delta N_2$ are therefore 83 and 89, respectively. In general, if m and n denote the possible numbers of ambiguity candidates for L1 and L2 double difference carrier phase respectively, the ambiguity search space can then be defined by

$$\Omega = \{(\nabla\Delta N_1^i, \nabla\Delta N_2^j) | i = 1, 2, \dots, m; j = 1, 2, \dots, n\} \quad (5.18)$$

5.2.2 Ambiguity Candidate Discrimination

Consider l consecutive epochs of double difference carrier phase observations. For each ambiguity candidate pair $(\nabla\Delta N_1^i, \nabla\Delta N_2^j)$ in the search space, the accumulated sum of squared residual is defined by

$$S_{i,j} = \sum_{k=0}^{l-1} (r_{i,j})_k^2 \quad (5.19)$$

where $r_{i,j}$ is the residual of the ionosphere-free combination with respect to this ambiguity pair and is given by

$$(r_{i,j})_k = (\nabla\Delta\Phi_{IF})_k - \nabla\Delta\mathbf{r}_k - \frac{c}{77f_1 - 60f_2} (77\nabla\Delta N_1^i - 60\nabla\Delta N_2^j) \quad (5.20)$$

If an ambiguity pair $(\nabla\Delta N_1^u, \nabla\Delta N_2^v)$ satisfies the following conditions:

$$S_{u,v} = \min(S_{i,j}) \quad (i = 1, 2, \dots, m; j = 1, 2, \dots, n) \quad (5.21a)$$

$$S_{p,q} = \min(S_{i,j}) \quad (i = 1, 2, \dots, m; j = 1, 2, \dots, n; i \neq u; j \neq v) \quad (5.21b)$$

$$\frac{S_{p,q}}{S_{u,v}} > \mathbf{t} \quad (5.21c)$$

then it is selected as the integer ambiguities subject to further confirmations such as misclosure test. The threshold \mathbf{t} is a predefined limit and it is usually can be set to 3. Figure 5.5 shows the accumulated sum of squared residual over time with respect to the correct ambiguity set and the incorrect ambiguity set, respectively. Although in the initial phase the incorrect ambiguity has smaller corresponding value, the correct ambiguity still can be picked out after a longer period of time.

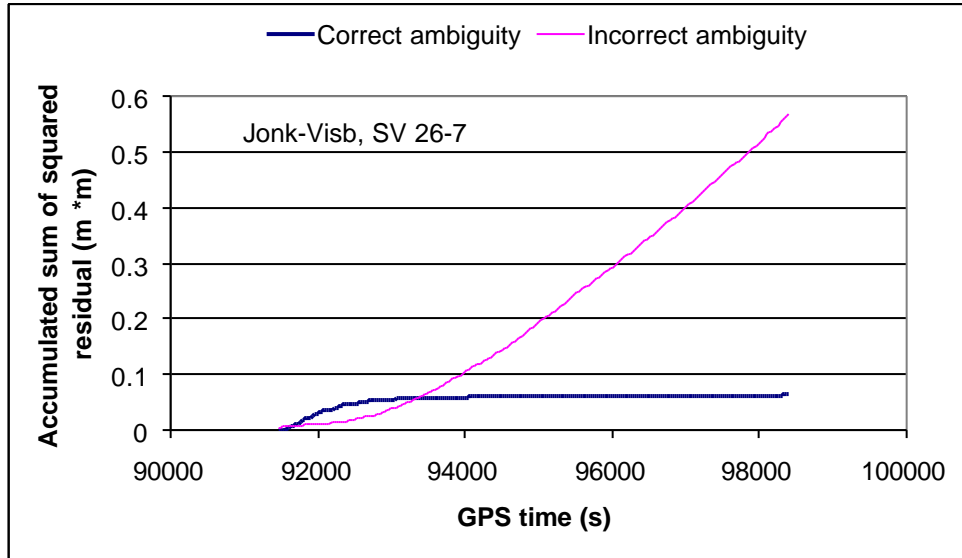


Figure 5. 5: Accumulated sum of squared residual for correct ambiguity and incorrect ambiguity.

5.2.3 Ambiguity Constraints

Wide-lane constraint

In order to further speed up the ambiguity resolution process, we use wide-lane ambiguity to reject those incorrect L1 and L2 ambiguity candidate pairs in the search space. The wide-lane carrier phase observation expressed in the following Eq. (5.28) has a wavelength of about 86cm. Therefore, its ambiguity can be much more easily resolved than L1 and L2 ambiguities whose wavelengths are 19cm and 24cm respectively.

$$\begin{aligned}\nabla\Delta\Phi_w &= \frac{f_1}{f_1-f_2}\nabla\Delta\Phi_1 - \frac{f_2}{f_1-f_2}\nabla\Delta\Phi_2 \\ &= \nabla\Delta\mathbf{r} + \mathbf{I}_w\nabla\Delta N_w + \frac{f_1f_2}{f_1^2-f_2^2}\nabla\Delta\mathbf{l} + \mathbf{e}(\nabla\Delta\Phi_w)\end{aligned}\tag{5.22}$$

where

$$\mathbf{I}_w = \frac{\mathbf{I}_1\mathbf{I}_2}{\mathbf{I}_2 - \mathbf{I}_1}\tag{5.23a}$$

$$\nabla\Delta N_w = \nabla\Delta N_1 - \nabla\Delta N_2\tag{5.23b}$$

If the wide-lane ambiguity can be correctly resolved, most of the L1 and L2 ambiguity pairs in the search space will not meet the criteria in Eq. (5.23b). Figure 5.6 shows that the search space consists of those grid points. The maximum number of valid L1 and L2 ambiguity pairs will be less than $\sqrt{n^2 + m^2}$ in total in terms of correct wide-lane ambiguity resolution. Consequently, the search space for L1 and L2 ambiguity candidates are significantly reduced by using the constraint of wide-lane ambiguity.

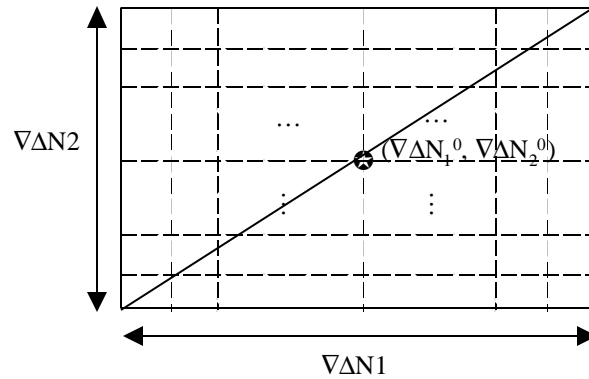


Figure 5. 6: Illustration of ambiguity search space.

If calculated ranges for $\nabla\Delta N_1$ and $\nabla\Delta N_2$ are 83 and 89, as derived in section 5.2.1, the maximum search space will be less than 122. Therefore, the search space is significantly reduced compared to the original search domain.

Misclosure constraint

A network misclosure test has also been implemented to reinforce the integrity of ambiguity resolution results. The principle of misclosure check is very simple: any number of baselines which form a closed loop must have zero ambiguity summation on L1 or L2 for any common satellite pair in the double difference. Some additional independent baselines are required to be resolved for this purpose. For instance, in a triangular loop composed by three baselines b_{AB} , b_{BC} and b_{CA} (shown in Figure 5.7), the ambiguities for any common pair of satellites should satisfy the conditions below:

$$N_{AB} + N_{BC} + N_{CA} = 0 \tag{5.24}$$

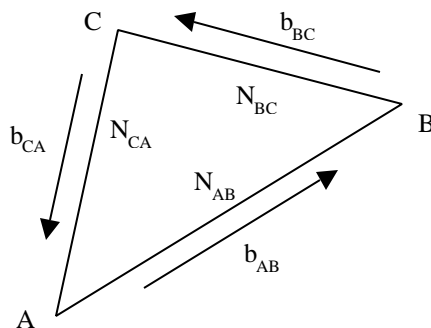


Figure 5. 7: Misclosure ambiguity check.

If the above condition is not satisfied, at least one of the baselines must have included incorrect ambiguity solutions. Further validations then have to be conducted under this situation.

5.3 CARRIER PHASE CYCLE SLIP DETECTION

Cycle slip causes the previous ambiguity to be no longer valid, as incorrect ambiguity will corrupt the estimation results and will probably lead to the Kalman filter divergence under severe situations. At reference stations, cycle slip may be caused by low signal-noise ratio, ionosphere irregularity or some other accidental events. Experience shows cycle slip seldom occurs under normal conditions when the elevation angle is higher than 15° , while it's likely to occur in lower elevation angles. Considering the much lower noise level in carrier phase even in low elevation angles, a cut off angle might be as low as 5° to supply more observation information. But cycle slip must be effectively detected when they occur. Repair can be made if the cycle slip can be reliably determined. Otherwise, the ambiguity resolution process needs to be reinitialized to resolve the changed ambiguity. Doppler measurement can be used for cycle slip detection due to its high accuracy. The phase increment between two consecutive epochs is firstly calculated by the difference between the carrier phase observable at the two epochs and then compared to the integration of the Doppler measurements during that interval. Cycle slip can be detected effectively by the consistency check between them. The phase increment between two consecutive epochs is

$$\Delta\Phi_i = \Phi_i - \Phi_{i-1} \quad (5.25)$$

The difference between direct phase increment and the Doppler integrated phase increment becomes

$$d\Phi_i = \Delta\Phi_i - (\dot{\Phi}_i + \dot{\Phi}_{i-1}) \cdot \Delta t \quad (5.26)$$

If $d\Phi_i$ exceeds a predefined threshold, cycle slip is considered to have occurred.

Figure 5.8 and 5.9 show the situation when cycle slip occurs. From the abrupt carrier phase jump and the Doppler measurement continuity, it's obvious that a cycle slip has occurred on the carrier phase measurements.

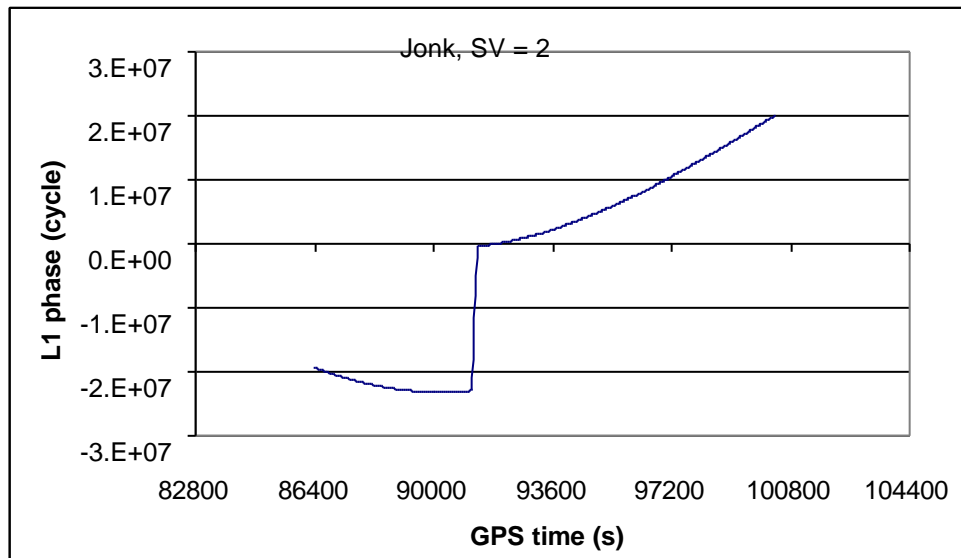


Figure 5. 8: Typical GPS cycle slip on L1 phase.

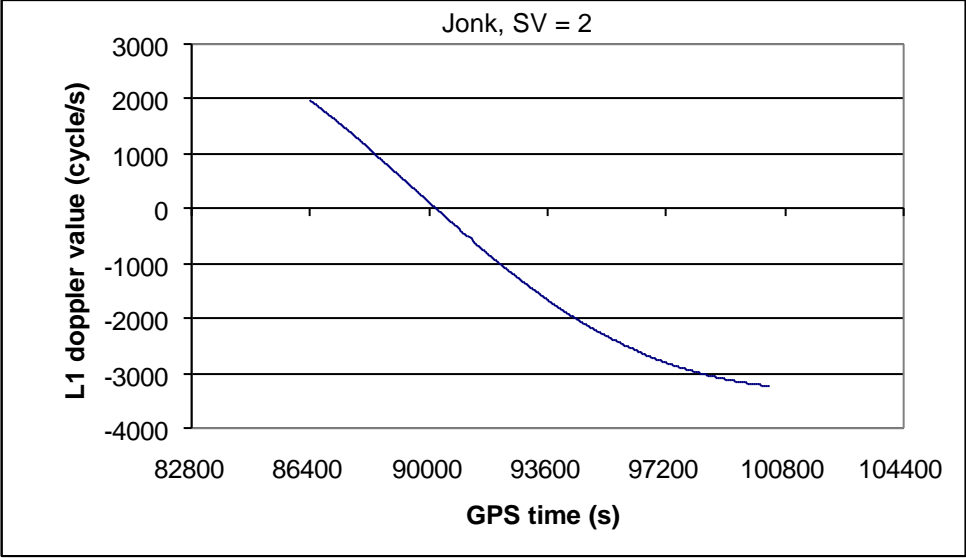


Figure 5. 9: The corresponding Doppler on L1.

CHAPTER 6

NUMERICAL RESULTS AND PERFORMANCE ANALYSIS

In this chapter, software development and numerical results will be presented using data from an operational regional area GPS network to assess the performance of the proposed ionosphere recovery method that has been described in Chapter 4 and Chapter 5.

6.1 SOFTWARE DEVELOPMENT

For the need of numerical analysis, a software package GPS Network based Ionosphere estimation (GNI) has been developed using C++ language to implement the proposed ionosphere recovery algorithms. Figure 6.1 shows the flowchart of the software for the implementation of the developed method. All the algorithms described in the previous chapters are integrated into the software and implemented in the corresponding functions. Although it is developed primarily for the case of regional area GPS network, it is also applicable for WADGPS or global-scale purpose with only minor modification in post-mission. Major functions include:

1. Troposphere modelling;
2. Wide-lane, L1 and L2 ambiguity resolution;
3. Single layer ionosphere model;
4. Streamlined Kalman filter;
5. Accuracy assessment.

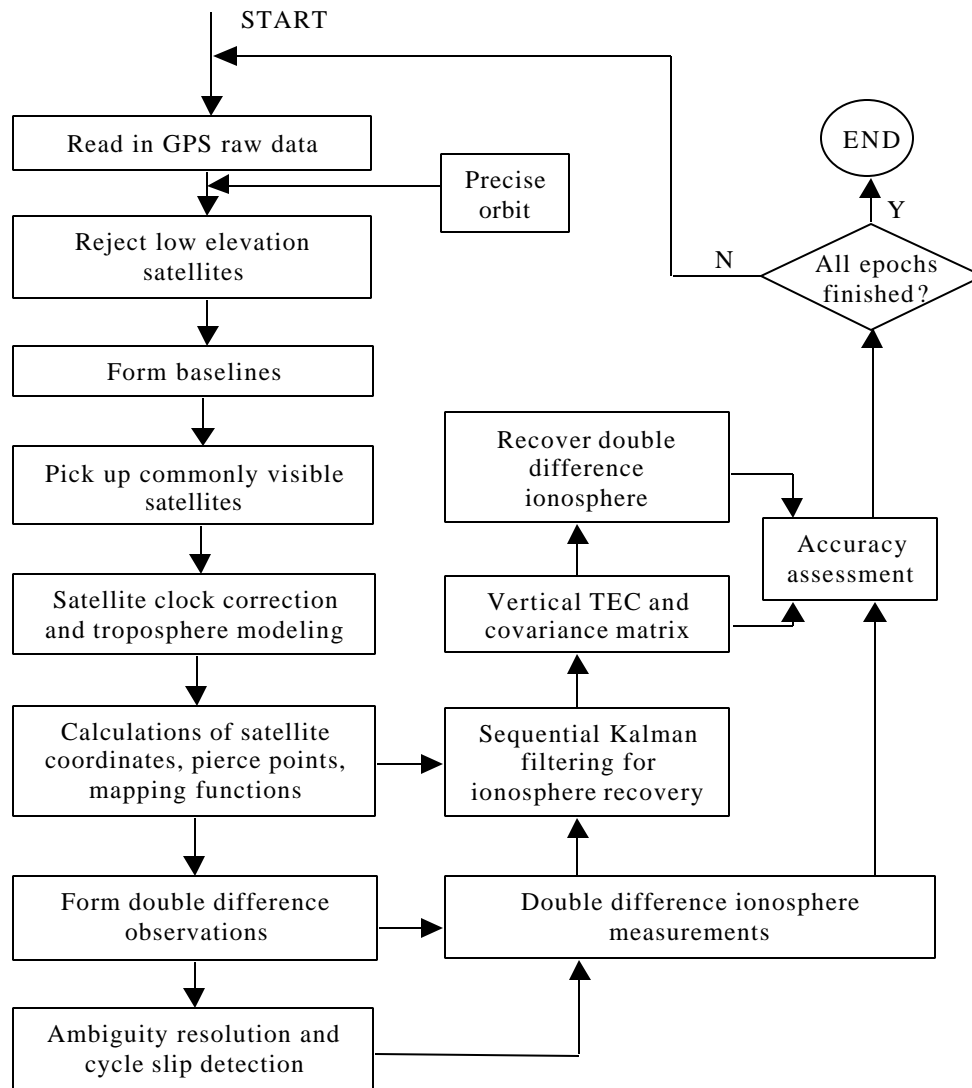


Figure 6. 1: Data processing flowchart of GNI software.

6.2 TEST DATA DESCRIPTION

6.2.1 SWEPOS Network

The Swedish GPS network (SWEPOS), as shown in Figure 6.2, has been in operation since August 1993. The SWEPOS network currently consists of 21 continuously operating GPS stations extended from latitude 55 to 69 degrees north with the average station separation of around 200km. It was established by the National Land Survey of Sweden (NLS) and Onsala Space Observatory (OSO) for applications such as crustal motion monitoring, real-time navigation and atmospheric monitoring. The SWEPOS network is furnished with a standard 3m tall steel-reinforced concrete pillar of circular cross-section and equipped with temperature-control. To make the center of the sphere coincide with the antenna, hemispheric plexi-glass radomes are mounted at each site. Each station is equipped with two Ashtech Z-XII dual frequency receivers which are connected to the same Dorne-Margolin antenna using a high quality power-splitting device. The network is operated and maintained by NLS and described in detail by Hedling and Jonsson [1996].

For the purpose of this research, ten stations in the southern areas, as shown in the blocked frame in Figure 6.2, were used to simulate a RADGPS network for numerical computations. The ten stations lie within the geographic latitude range from 55°N to 60°N, and from 11°E to 18°E in the geographic longitude. The solid lines shown in Figure 6.3 are nine independent baselines available in the network when the station Jonk is used

as the base reference station. The baseline length ranges from about 100km to 400km. The dashed lines are baselines whose ambiguities will also be determined so that they can be used to form closed-loops with those solid baselines for network misclosure check during ambiguity resolution but they will not be included for ionosphere estimation.

All the data collected are in RINEX format, with observations including C/A code, dual-frequency P code, dual-frequency carrier phase, dual-frequency Doppler output. For our use, dual-frequency P code and carrier phase are used while L1 Doppler is used for cycle slip detection. The data was originally collected in the update rate of 1HZ. For our purpose, it is re-sampled at a 30 seconds rate. In total, 32 continuous hours of data (on May 17-18, 1999) from the ten GPS stations was used for our testing. The global 3-hour geomagnetic index Kp values, which are an indicator of high latitude (auroral and sub-auroral regions) ionospheric activities, were 0, 0₊, 0₊, 1₀, 0₊, 1₀, 1₀, 0₊, 4₋, 4₀, 4₀ for the whole time period. It indicates the ionosphere was quiet during the period. The broadcast ephemeris was not used. Instead, the precise orbit is downloaded from the IGS website service. The precise coordinates of all the ten stations are provided as well. There are no troposphere parameters (i.e. meteorological observations) provided although they are preferred in order to ensure a minimum level of troposphere residual during ambiguity resolution.



Figure 6. 2: SWEPOS GPS network.

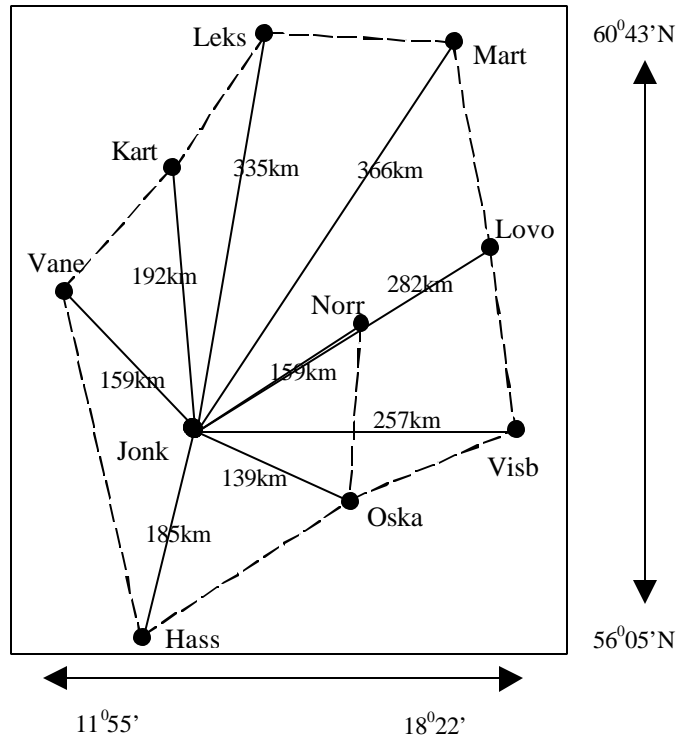


Figure 6. 3: Baseline configuration.

6.2.2 Satellite Availability

At the time when the data were collected from the network on May 17-18, 1999, there were total 27 GPS satellites in space that were healthy and providing services. For each formed baseline, the available satellites are those commonly visible to both reference stations of the baseline. Figure 6.4 shows the number of those commonly visible satellites observed by all the ten GPS stations. From the figure, the number of the visible satellites ranges from 4 to 10 while most of the time, there are about 6-8 visible satellites. Since so many satellites are visible at any given time as observed by the whole network, it provided sufficient observations to recover the ionosphere over the network.

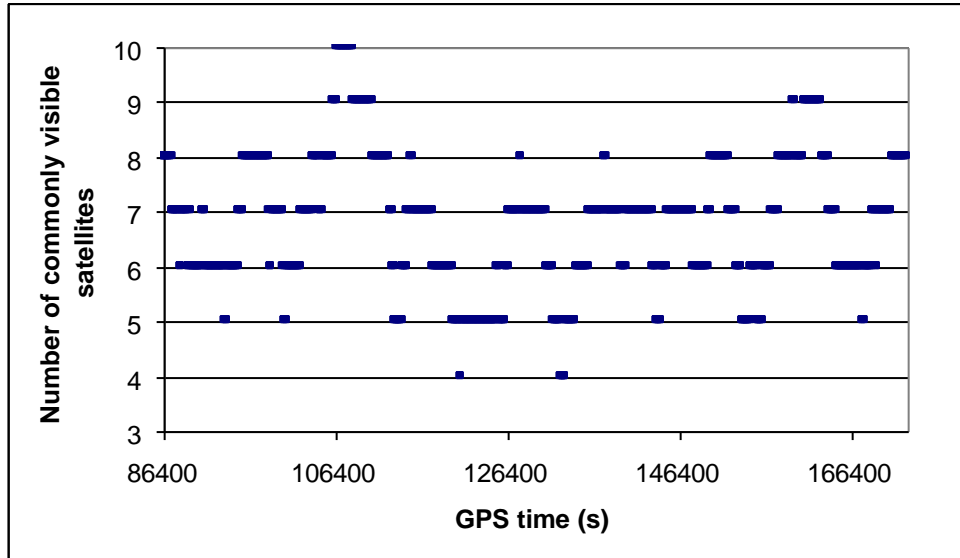


Figure 6. 4: Number of the commonly visible satellites for the whole network.

6.3 CODE-DERIVED SLANT IONOSPHERE ANALYSIS

As the receiver at each station is a dual-frequency GPS receiver, the pseudorange or phase observations on L1 and L2 can be used to directly monitor the ionosphere change trend over the observing site. Figure 6.5 shows the slant ionosphere delays (on L1) derived from pseudorange, combined pseudorange and carrier phase, pure phase observations respectively. The code-derived ionosphere is much noisier than the smoothed one derived from the combined code and phase measurements although their trends are matching very well. The phase-derived ionosphere delay has an offset compared to the smoothed one by an unknown ambiguity. The approximate vertical ionosphere delay is also calculated from the slant delay divided by a slant factor which is elevation-related. The vertical ionosphere delay varies in several metres due to the corruption of the L1/L2 satellite/receiver instrumental bias which is also mapped to the vertical direction. Figure

6.6 shows all the slant ionosphere delays (on L1) observed at the station of Jonk for the whole period of thirty two hours. All the satellites above the cutoff angle of 15 degrees have been picked up. Although the L1/L2 instrumental biases are not removed from the ionosphere delays, the ionosphere diurnal change can still be seen. When estimating ionosphere in non-difference mode using the mixed pseudorange and phase observations, the instrumental biases have to be considered as unknowns to be estimated at the same time, even though the ionosphere parameters are the major concern.

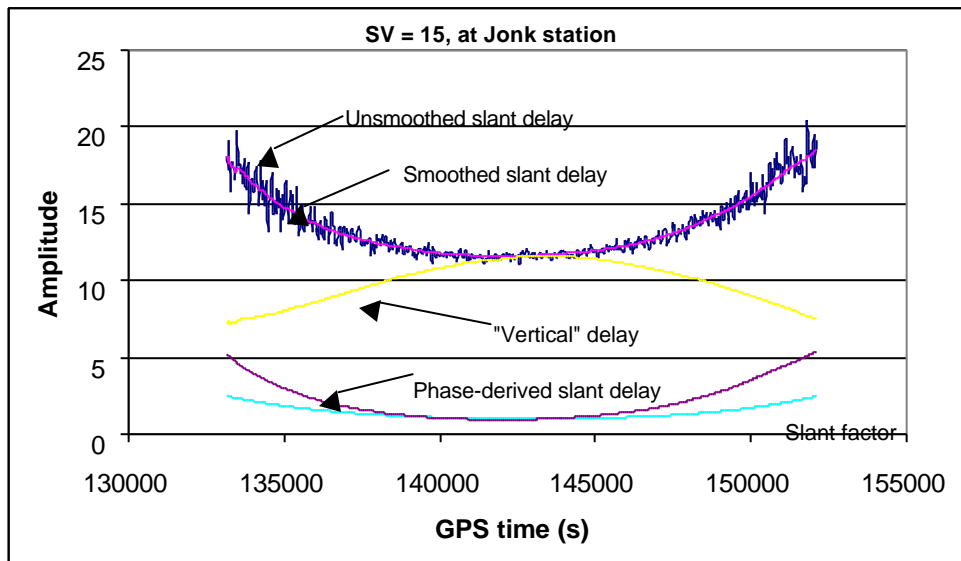


Figure 6. 5: Ionosphere delay without bias removed (m).

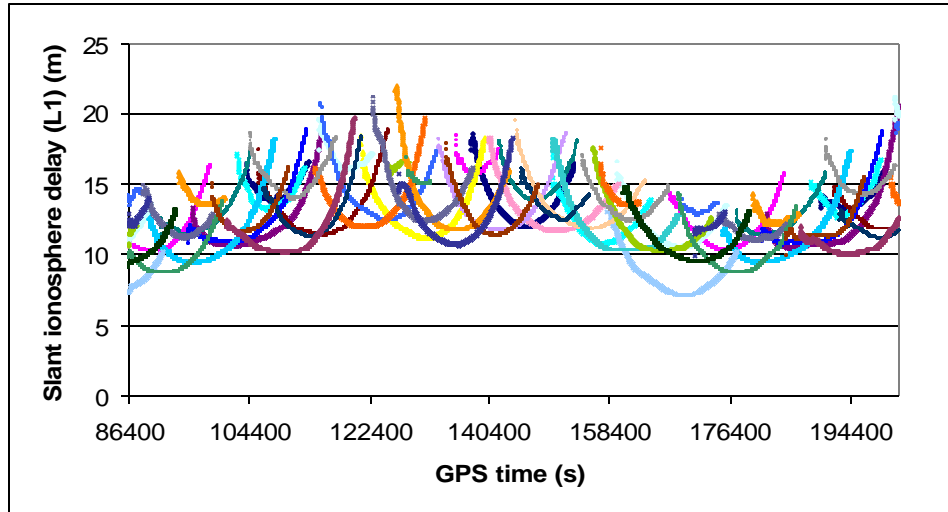


Figure 6. 6: Slant ionosphere delay (on L1) at Jonk (without L1/L2 instrumental bias removed), on May 17-18, 1999.

6.4 AMBIGUITY RESOLUTION RESULTS

Ambiguity resolution over long baseline is one of the most challenging tasks during the ionosphere recovery, which is much more difficult than that in the case of short baselines. To ensure the quality of the double difference measurements, the cutoff angle of the reference satellite is selected as 30 degrees in this thesis. For the whole network in the time duration of thirty-two hours, there are about one thousand double difference ambiguities to be resolved in total. In our testing, the ambiguities can be resolved in most cases using the proposed method described in Chapter 5. Presented in Table 6.1 is a brief summary of ambiguity resolution results. Some ambiguities are difficult to resolve because the troposphere residual error still largely remains in certain circumstances after modelling which makes the ambiguity discrimination more difficult. In general, the

shorter the baseline, the easier the ambiguity resolution, which can be observed clearly from the table.

Table 6. 1: Ambiguity resolution summary from the whole network.

Baseline name	Baseline length (km)	Total ambiguities	Ambiguities resolved	Successful rate(%)
Jonk – Vane	159	123	110	89.4
Jonk – Karl	192	124	102	82.3
Jonk – Leks	335	119	95	80.0
Jonk – Mart	366	117	86	73.5
Jonk – Lovo	282	120	97	80.8
Jonk – Visb	257	115	94	81.7
Jonk – Oska	139	120	109	90.8
Jonk – Hass	185	123	103	83.7
Jonk – Norr	159	121	112	92.6

The troposphere model can be further improved if station meteorological data is available such as temperature, pressure and humidity measurements. It is expected the use of measurements from the water vapor radiometers can further facilitate the ambiguity resolution process.

6.5 PHASE-DERIVED DOUBLE DIFFERENCE IONOSPHERE MEASUREMENT ANALYSIS

As double difference ionosphere measurements are our major information sources to recover the ionosphere, their quality should be ensured. This section will present the phase-derived double difference ionosphere measurements. A comparison with the code-derived double difference ionosphere is also performed to examine the consistency between them.

6.5.1 Phase-derived Double Difference Ionosphere

From the Eq. (4.5), we can see that the double difference ionosphere measurements are only affected by the phase multipath and measurement noise if the ambiguities are correctly determined. The multipath and measurement noise are considered at a negligible level at the reference sites equipped with high quality GPS receivers.

For those phase observations whose ambiguities can't be resolved, the corresponding double difference ionosphere delays are not included in the ionosphere estimation. Since there are many redundant measurements, the quality of the resulting estimates will not be affected in lack of these measurements provided that the system states are sufficiently observable.

Given in Figures 6.7 – 6.15 are the double difference ionosphere measurements for all the nine independent baselines (shown as the solid lines in Figure 6.3) using the dataset of thirty-two hours from 00AM on May 17 to 08AM on May 18, 1999. The double difference ionosphere measurements are derived after the ambiguities are correctly resolved using the methods described in this research. These double difference ionosphere measurements range within several tens of centimetres, usually as a function of the baseline length. Table 6.2 shows the absolute average double difference ionosphere delays for each baseline. It can be seen from the figures that the longer the baseline the weaker the spatial correlation of the ionosphere and the larger the level of the double difference ionosphere. Note also that the diurnal behavior in the undifferenced ionosphere is not obviously shown in the double difference ionosphere. All the double difference ionosphere measurements from these baselines except Jonk-Norr are included in the vertical TEC estimation, while those measurements from Jonk – Norr will be used as an independent source for accuracy assessment of the recovered vertical TEC estimates.

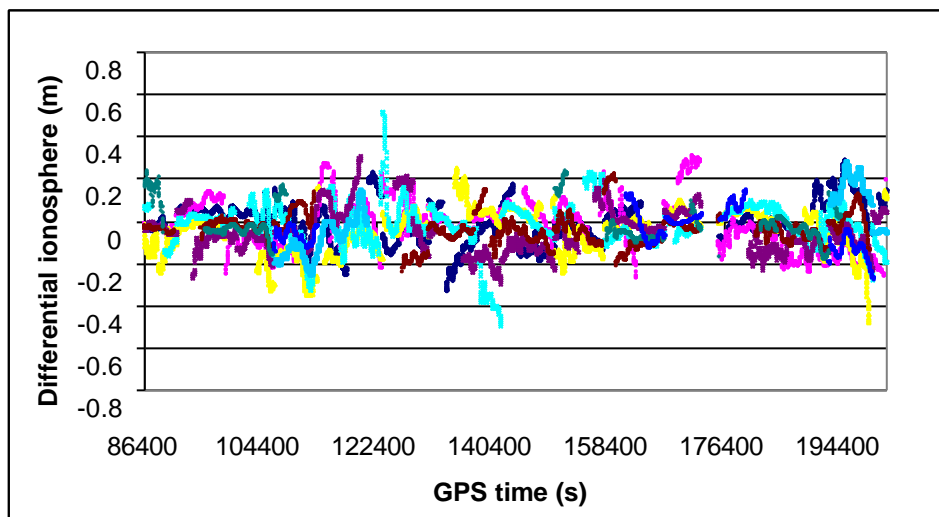


Figure 6. 7: Double difference ionosphere measurement for Jonk-Vane (159km)

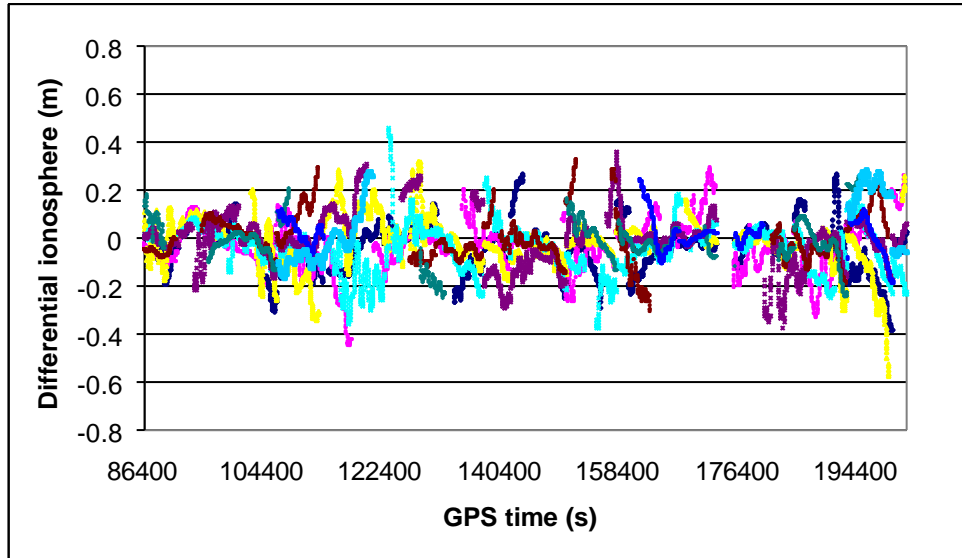


Figure 6. 8: Double difference ionosphere measurements for Jonk-Kart (192km).

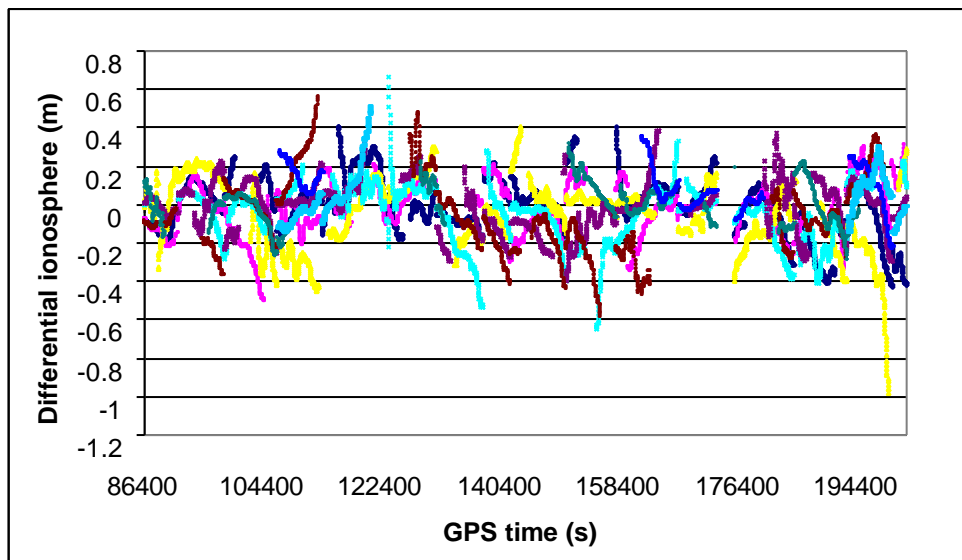


Figure 6. 9: Double difference ionosphere measurements for Jonk-Leks (335km).

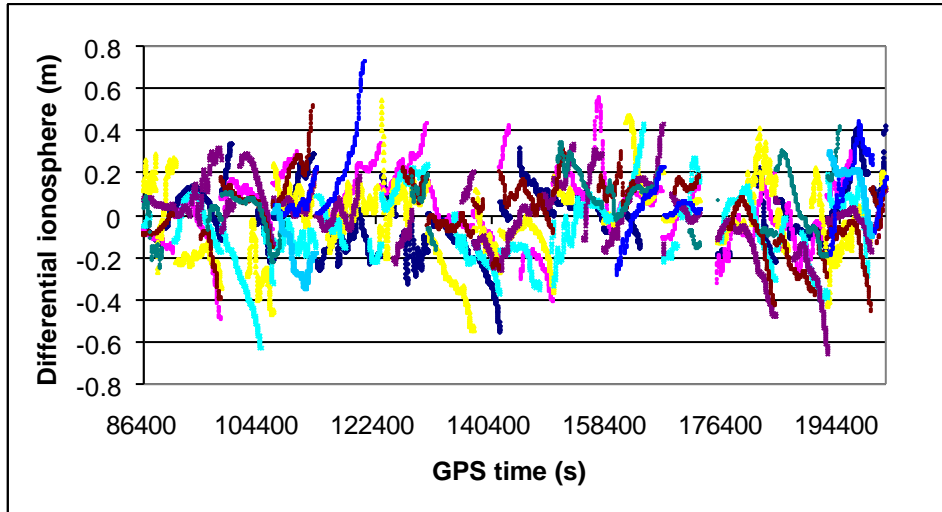


Figure 6. 10: Double difference ionosphere measurements for Jonk-Mart (366km).

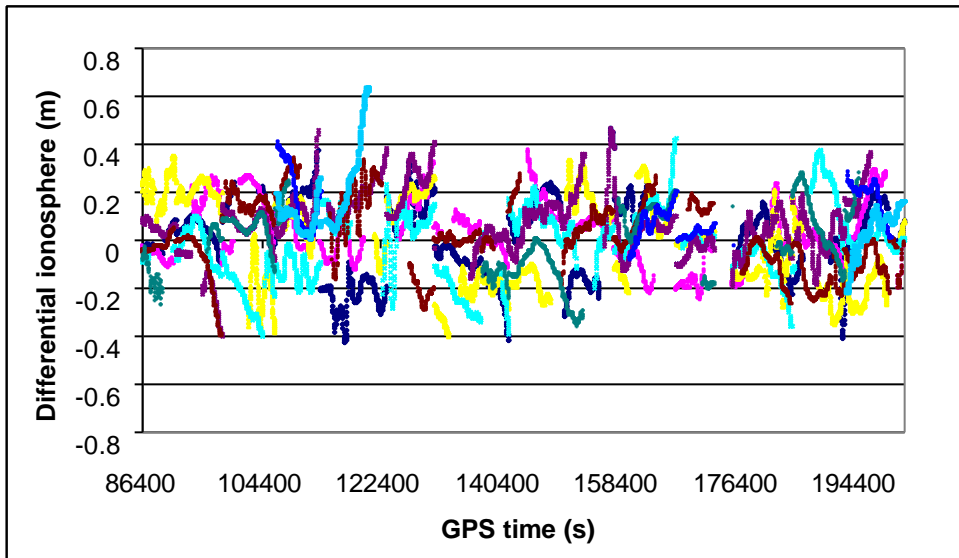


Figure 6. 11: Double difference ionosphere measurements for Jonk-Lovo (282km).

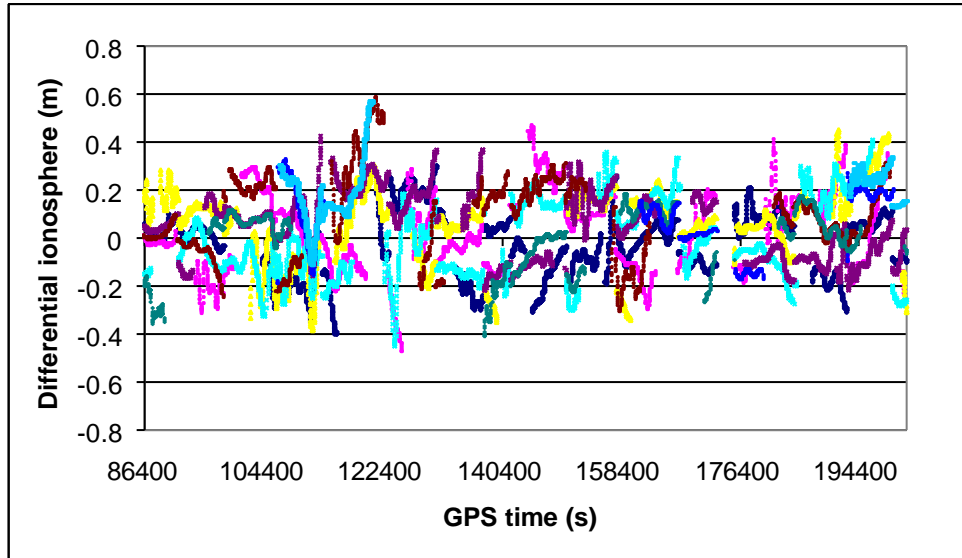


Figure 6. 12: Double difference ionosphere measurements for Jonk-Visb (257km).

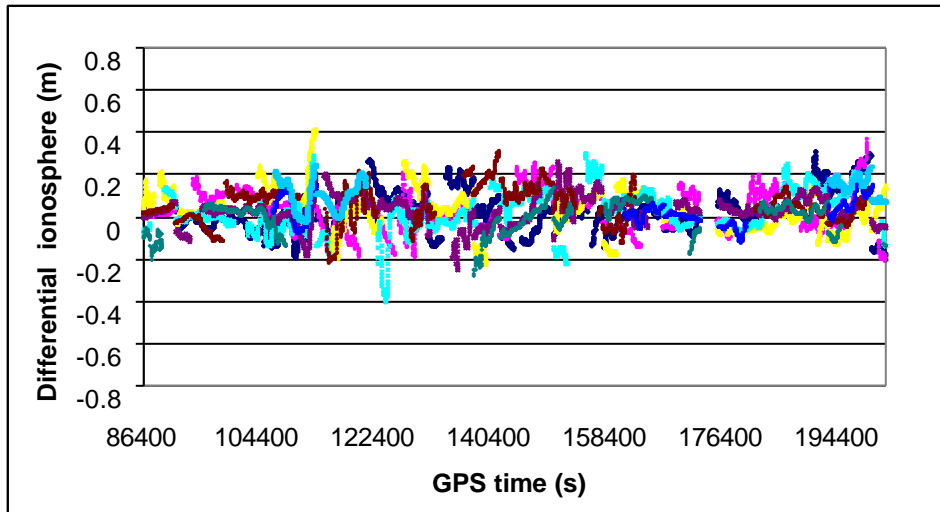


Figure 6. 13: Double difference ionosphere measurements for Jonk-Oska (139km).

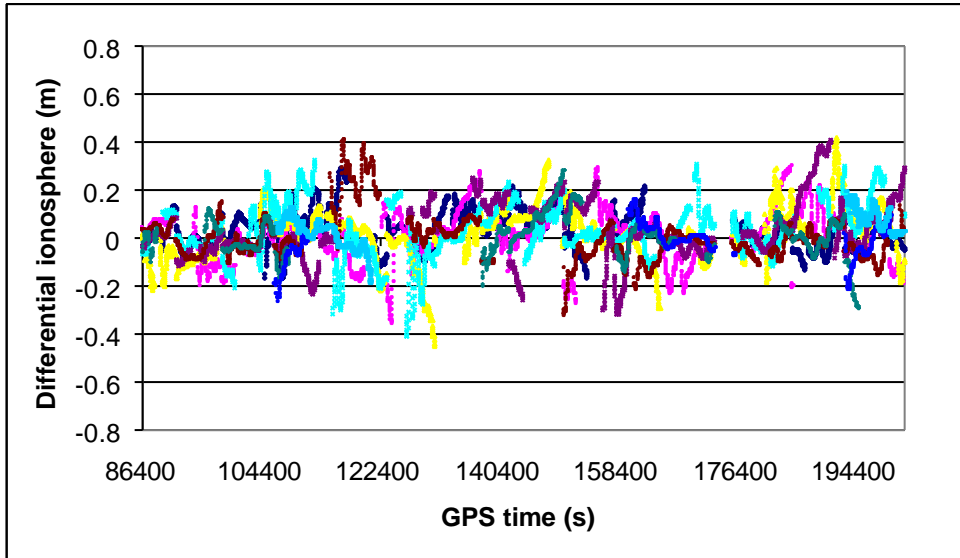


Figure 6. 14: Double difference ionosphere measurements for Jonk-Hass (185km).

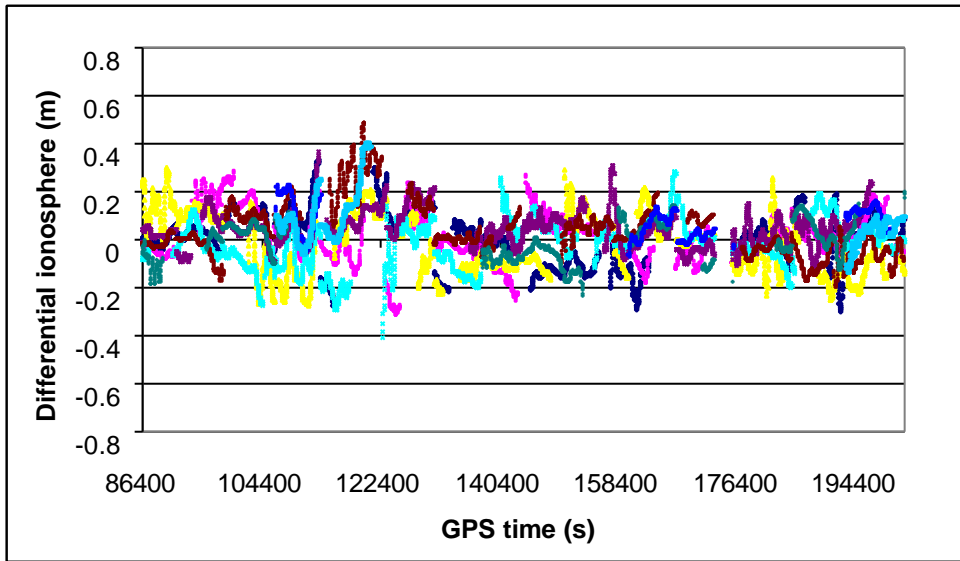


Figure 6. 15: Double difference ionosphere measurements for Jonk-Norr (159km).

Table 6. 2: Mean of the double difference ionosphere delay for all the baselines

Baseline name	Baseline length (km)	Mean of absolute DD. iono. (cm)
Jonk – Vane	159	13.3
Jonk – Karl	192	15.1
Jonk – Leks	335	18.3
Jonk – Mart	366	21.7
Jonk – Lovo	282	17.4
Jonk – Visb	257	16.8
Jonk – Oska	139	14.6
Jonk – Hass	185	15.8
Jonk – Norr	159	14.8

6.5.2 Comparison between Phase-derived and Code-derived Double Difference Ionosphere Measurements

In the ionosphere recovery, we use the carrier phase derived double difference ionosphere as the measurement after ambiguities are resolved. The double difference ionosphere can also be derived using dual-frequency pseudorange observations combined with carrier phase measurements. Although the code-derived ionosphere is not used as the principal observable in the ionosphere recovery, we can use it to compare with the carrier phase derived one. It helps us to examine the consistency between these two measurements.

Considering the dual-frequency pseudorange and carrier phase observable, the ionosphere delay can be explicitly contained by

$$P_1 - P_2 = -I + b_P - B_P + e(P_1 - P_2) \quad (6.1a)$$

$$\Phi_1 - \Phi_2 = I + \mathbf{l}_1 N_1 - \mathbf{l}_2 N_2 + b_\Phi - B_\Phi + e(\Phi_1 - \Phi_2) \quad (6.1b)$$

In the above equations, the satellite/receiver L1/L2 instrumental biases are considered as constants for both pseudorange and carrier phase. For each satellite, the ambiguities are constant provided no cycle slip occurs. Considering the noisy ionosphere derivation from the pseudorange, we use the carrier phase derived ionosphere in Eq. (6.1b) to smooth the pseudorange-derived ionosphere in Eq. (6.1a). Note the ionosphere derivation is corrupted by the instrumental bias.

The smoothed but instrument-biased non-difference ionosphere can be calculated as follows:

The initial estimate:

$$\tilde{I}_0 = -(P_1 - P_2)_0 \quad (6.2a)$$

$$\mathbf{s}_{\tilde{I}_0}^2 = \mathbf{s}_{(P_1 - P_2)_0}^2 \quad (6.2b)$$

The estimate at k-th epoch:

$$(w_1)_k = \frac{1}{\mathbf{s}_{(P_1 - P_2)_k}^2} \quad (6.3a)$$

$$(w_2)_k = \frac{1}{\mathbf{s}_{\tilde{I}_{k-1}}^2 + \mathbf{s}_{\mathbf{d}(\Phi_1 - \Phi_2)_k}^2} \quad (6.3b)$$

$$\begin{aligned} (\tilde{I})_k = & -\frac{(w_1)_k}{(w_1)_k + (w_2)_k} (P_1 - P_2)_k \\ & + \frac{(w_2)_k}{(w_1)_k + (w_2)_k} [\tilde{I}_{k-1} + \mathbf{d}(\Phi_1 - \Phi_2)_k] \end{aligned} \quad (6.3c)$$

$$\mathbf{s}_{\tilde{I}_k}^2 = \frac{1}{(w_1)_k + (w_2)_k} \quad (6.3d)$$

where

$$\mathbf{d}(\Phi_1 - \Phi_2)_k = (\Phi_1 - \Phi_2)_k - (\Phi_1 - \Phi_2)_{k-1} \quad (6.4)$$

As the L1/L2 instrumental biases are stable and they can be considered as constants, they are cancelled out after double difference, thus we get the double difference ionosphere:

$$\nabla \Delta I_{AB}^{ij} = (\tilde{I}_A^i - \tilde{I}_B^i) - (\tilde{I}_A^j - \tilde{I}_B^j) \quad (6.5)$$

which is only contaminated by the remaining multipath and noise errors which have a random error behavior.

Figures 6.16 and 6.17 show two typical examples of such kind of comparison. It is clear that the overall changing patterns of the carrier phase derived and pseudorange derived double difference ionosphere are matching, whereas the latter is apparently much noisier than the former one.

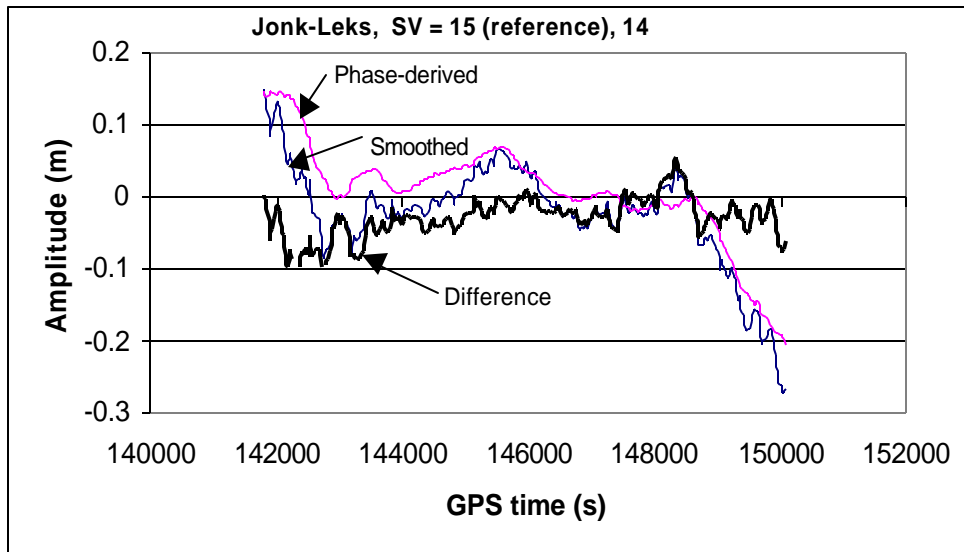


Figure 6. 16: Comparison of carrier phase derived and pseudorange derived double difference ionosphere (1).

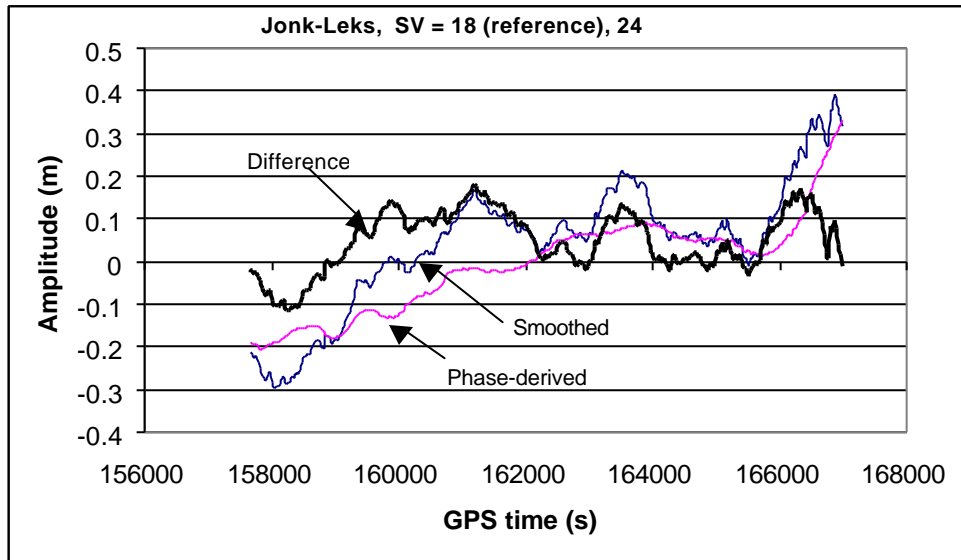


Figure 6. 17: Comparison of carrier phase derived and pseudorange derived double difference ionosphere (2).

6.6 IONOSPHERE PIERCE POINT DISTRIBUTION

Figure 6.18 shows the pierce points of all the double difference ionosphere measurements observed by the ten GPS stations during a whole day time period (GPS time: 86400s – 172800s, on May 17, 1999) when a cutoff angle of 15 degrees was used. Although the ground GPS stations are located from about 56°N to 60°N in geographic latitude, the pierce points are lying in a geomagnetic latitude band from 45°N to 70°N on the ionosphere shell. This is due to the facts that the ionosphere shell is above the Earth at 350km and the satellites are moving continuously. As shown in the figure, the distribution of the pierce points is dense in the middle of the band but becomes gradually sparser at latitude away from the centre of the network. Therefore, the recovered vertical

TEC will be more accurate for grid points located in the middle of the band while gradually degraded as the grid points move away from the middle areas. The geomagnetic local hour angle in the later part of the figure is not in the range of 0 ~ 360 degrees, in order to avoid the overlap with that in the previous day.

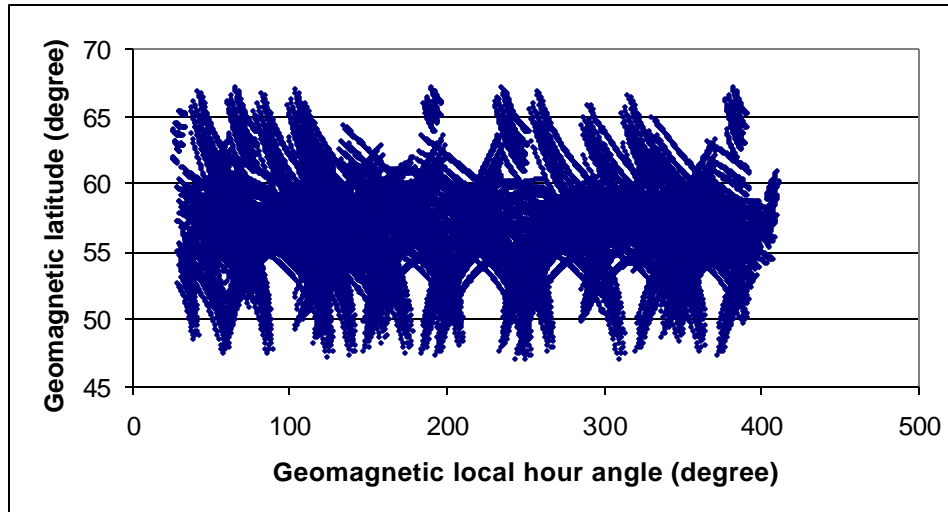


Figure 6. 18: Geomagnetic latitude band of pierce points on ionosphere shell.

6.7 IONOSPHERE RECOVERY RESULTS AND ANALYSIS

The resulting vertical TEC estimates and the corresponding standard deviation values of the vertical L1 delay for the selected thirty-two hours' data period are shown in Figure 6.19 and Figure 6.20. The coverage is from 53°N to 60.5°N in geomagnetic latitude. The recovered vertical TEC values show clearly the diurnal change of the ionosphere except some less accurate values at the beginning and at the end of the data time due to the fact that the grid points were actually new states in the filter with insufficient observations during those short periods. At different geomagnetic latitudes the vertical TEC estimates

are quite tight since we have used a small grid size and these grid points are close in geomagnetic locations. The standard deviation is only a few centimetres for most of the grid points, while the large values at the beginning and at the end of the data time are obviously caused by the insufficient available measurements during those periods.

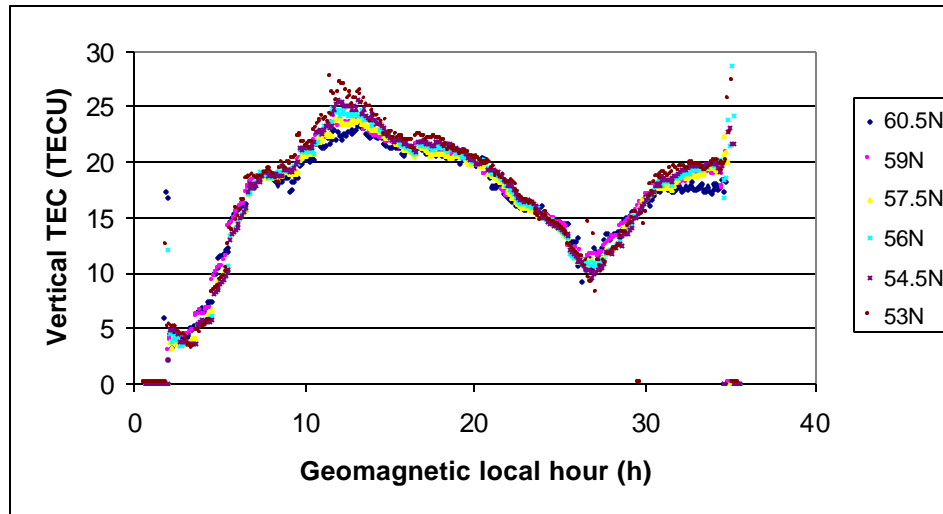


Figure 6. 19: Recovered vertical TEC in regional area (geomagnetic latitude range of 7.5 degrees).

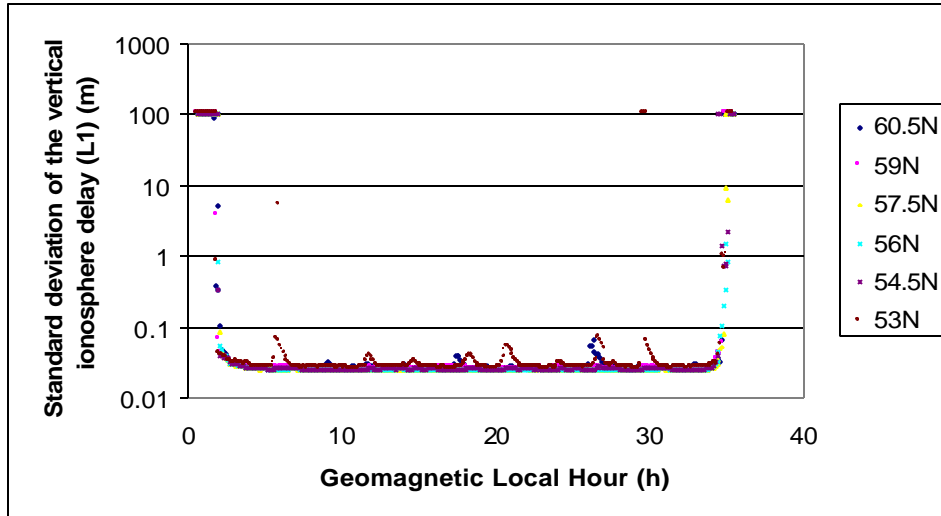


Figure 6. 20: Standard deviation of the vertical ionosphere delay (on L1).

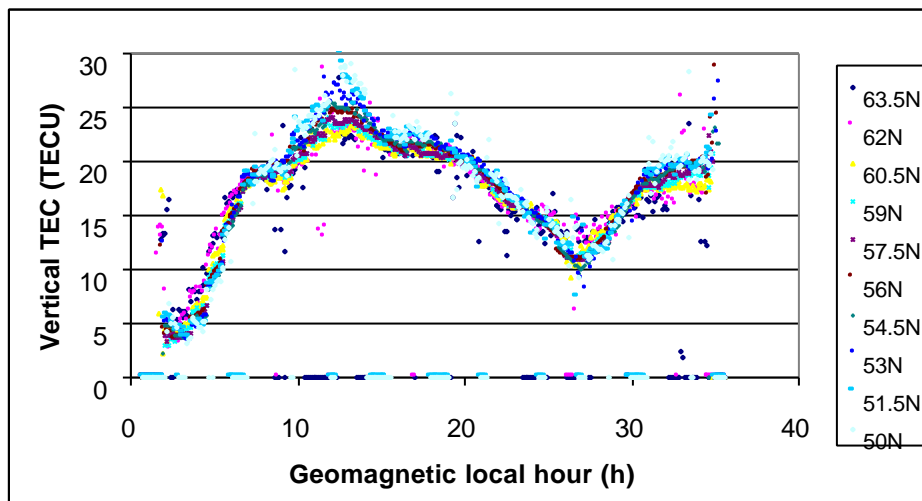


Figure 6. 21: Recovered vertical TEC in regional area (geomagnetic latitude range of 13.5 degrees).

Figure 6.21 shows the vertical TEC values at the grid vertices on different geomagnetic latitudes in a range of 13.5 degrees from 50°N to 63.5°N. It is clear that the vertical TEC values at some vertices in the boundary latitude are deviating away from the “truth”. The

overall variation of the vertical TEC values in this range is much greater than that in the medium areas of the 7.5-degree latitude band. The phenomenon coincides with the pierce point distribution illustrated in Figure 6.18 from which we can see there are sufficient pierce points covering the geomagnetic latitude band between 53°N and 60°N without evident blank areas. Therefore, the obtained vertical TEC estimates are much more accurate within that range. In the lower or upper geomagnetic latitude areas with less sufficient pierce points of ionosphere measurements, degradation was experienced in the estimations results. The zero values in the figure are for those grid points which have no observations for updating thus remain in the initial values.

From the recovered vertical TEC values in the figures, it is noted that the TEC values during the night-time are not as uniform as expected. This might be related to seasonal change of ionosphere. It is found that during the period of a whole year, the behavior is different from month to month and even different within a specific month; the ionosphere is not day-to-day homogeneous. In some seasons, the ionosphere is not necessary to be flat in the night time. Also it should be noted that the region is slightly below the auroral region where the ionosphere behavior is more complicated and more difficult to predict.

6.8 PERFORMANCE ANALYSIS

To assess the accuracy of the estimated vertical ionosphere delay, two methods can be utilized. One is to check directly the value of the associated variance value from the covariance matrix. Since the pierce points are not distributed evenly on the thin shell, the

resulting accuracy will therefore be at an uneven level at different grid points. The variance of any vertical TEC estimate, however, does not necessarily indicate the actual accuracy. This is due to the fact that the variance is not dependent on the observations but is a function of several factors, e.g., the assumed ionosphere model and the assumed noise level of the measurements, while these assumptions may deviate from the truth to some extent. Although there exist the above limitations to use variance for accuracy assessment, it still can be used to assess the filter's performance such as convergence. A small variance indicates the associated vertical TEC estimate has converged after continuously updating using sufficient measurements over time.

Another assessment that can be conducted is the consistency check. After the absolute vertical TEC is recovered, the double difference ionosphere delay can be re-calculated from the estimates, different from the way which uses the network observations to derive the double difference ionosphere after the ambiguities are resolved. As the latter contains no modelling errors, it can be employed as the reference. The accuracy of the recovered double difference ionosphere delay therefore can be assessed through a comparison to the reference. For our case, one of the baselines has been purposely not included in the ionosphere recovery estimation process and this baseline can then be used to conduct an independent quality assessment of the vertical TEC estimates. Such consistency checks are also conducted for those baselines which are included in the process of vertical TEC estimation. To demonstrate the obtainable accuracy of the ionosphere recovery, only those double difference ionosphere delays whose pierce points lie within the central area of the latitude band and whose associated vertical TEC estimates have all converged at

the comparison epoch are included in the consistency testing. The accuracy assessment of the estimated vertical TEC thus contains two steps:

- 1) first forming double differenced ionosphere using the recovered absolute ionosphere TEC values;
- 2) and then comparing the recovered double difference ionosphere with the directly measured double difference ionosphere based on data from all the baselines including an independent baseline, i.e. Jonk-Norr, which was not included in the vertical ionosphere estimation.

In this testing, the data from the Norr station has not been used in our ionosphere estimation. The double difference ionosphere measurements derived from the baseline Jonk-Norr therefore can be used as external measurements to assess if the absolute ionosphere has been precisely determined. In addition, the double difference ionosphere measurements from other eight baselines are also compared for internal consistency assessment. Figure 6.22 shows the probability distribution of the differences between the originally measured and recovered double difference ionosphere for all the nine independent baselines. From the figure, we see that most differences fall within a small neighborhood close to zero. The corresponding RMS values are provided in Table 6.3 and they all are at the centimetre level. The results are quite consistent including baseline Jonk-Norr whose data has not been used in the ionosphere recovery computations. The RMS from the baselines of Jonk-Leks, Jonk-Mart, Jonk-Lovo and Jonk-Visb are slightly larger than the other baselines because of their relative longer baseline length. This confirms the correctness of the ionosphere recovery results using the method proposed in this research.

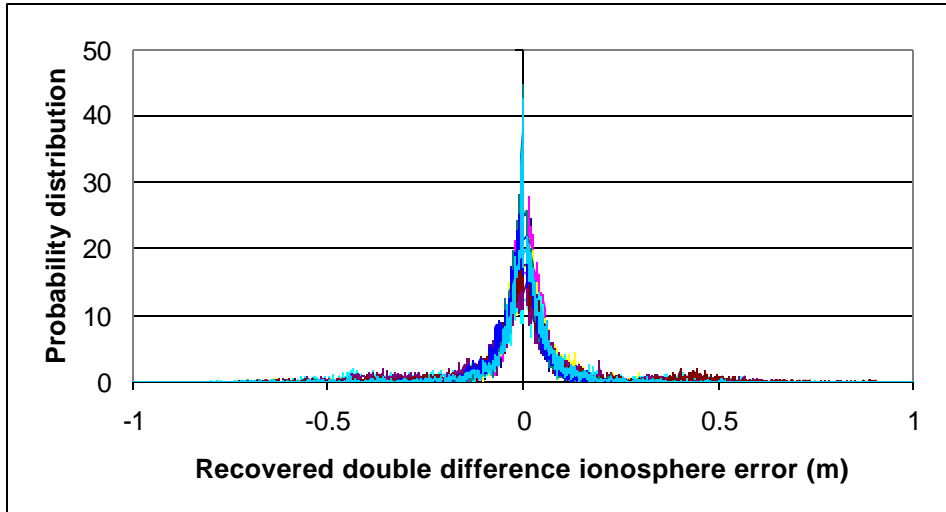


Figure 6. 22: Error distribution of the ionosphere estimates.

Table 6. 3: RMS of the recovered double difference ionosphere.

Baselines	RMS (cm)
Jonk – Vane	4.6
Jonk – Karl	4.4
Jonk – Leks	6.1
Jonk – Mart	6.9
Jonk – Lovo	6.6
Jonk – Visb	6.9
Jonk – Oska	4.6
Jonk – Hass	5.1
Jonk – Norr	5.8

CHAPTER 7

CONCLUSIONS AND RECOMMENDATIONS

The major objective of this thesis is to develop a new method of ionosphere recovery based on a regional area GPS network using carrier phase as the principal observable. The thesis is composed of two parts. The relevant theory on GPS, ionosphere characteristics and their inter-relationship was included in the first part, combined with a brief review of some previous work. The second part consists of the development of a new ionosphere estimation methodology, which focuses on ionosphere modelling and long-baseline ambiguity resolution. A single layer ionosphere band concept and a streamlined Kalman filter were developed for ionosphere recovery over regional area GPS networks. An ambiguity resolution approach has been developed which is appropriate over long baselines. A software package has also been developed for the implementation of the proposed method. Data from the SWEPOS regional GPS network was used for numerical analysis to assess the performance of the proposed regional area ionosphere recovery method. In the following, conclusions are drawn from this research and recommendations are given for future work.

CONCLUSIONS

- 1) A new ionosphere recovery method has been developed in this thesis which is based on a banded single layer ionosphere grid model described in the solar-geomagnetic coordinate system. To account for the movement of the GPS network stations with

respect to the solar-geomagnetic system, a slide window was imposed on the ionosphere shell to include the ionosphere which was only visible to the regional area GPS network stations. The updating was implemented on the ionosphere grid points within that window.

- 2) A streamlined Kalman filter has been designed to estimate the vertical ionosphere TEC above the regional area GPS network. The sequential processing procedure of the filter has reduced the computational complexity of the ionosphere estimation. The filter uses the double difference carrier phase observable to determine the absolute vertical TEC of the grid points. From the internal and external consistency examination results, the vertical TEC estimates can reach an accuracy of several centimetres in the dense pierce point distribution areas on the ionosphere shell.
- 3) Compared to WADGPS, the RADGPS network has been demonstrated to have higher accuracy and higher spatial resolution. With the sparse GPS station configuration, WADGPS usually employs a $5^{\circ} \times 5^{\circ}$ grid size with the vertical TEC estimation accuracy in metre level. In contrast, a dense RADGPS network can allow for a $1.5^{\circ} \times 1.5^{\circ}$ or even smaller grid size with the resulting centimetre level accuracy in vertical TEC estimates.
- 4) A long baseline ambiguity resolution method has been developed for the use of carrier phase observable in ionosphere recovery. With the focus on ionosphere, the orbit and troposphere effects have been eliminated to a negligible level using IGS

precise ephemeris and Saastamoinen-Niell troposphere modelling. However, the success rate of the method is dependent on the effectiveness of an appropriate troposphere model. Accumulated sum of residual square is used in ambiguity discrimination combined with wide-lane ambiguity and misclosure constraint.

- 5) A software package GPS Network based Ionosphere estimation (GNI) has been developed to implement the proposed method. The software can do post-mission processing using carrier phase, and real-time ionosphere estimation using carrier phase and code combination measurements.

RECOMMENDATIONS

- 1) Since the proposed method uses double difference measurements as the principal observable, one or more longer baselines are preferred to be included in those independent baselines to avoid the possible weak geometry. However, ambiguity resolution will become more difficult in this case. A balance between them must be carefully considered. Optimization of baseline configuration should thus be included in the future work.
- 2) The proposed method estimates the vertical TEC solely dependent on the measurements. No inter-correlation between the grid points is considered in the ionosphere dynamic model although such a correlation exists. A collocation approach

integrated into the dynamic model may lead to a more robust solution which should be considered in the future.

- 3) Although the single layer model is appropriate to simplify the ionosphere modelling, it has some limitations in nature. The fixed 350 km ionosphere shell height may not be the height of maximum electron density since the latter is in reality varying at different geographic locations. Since the ionosphere has peak activities in recent years, the distribution of electron density would be more complicated and unpredictable. In this situation, a three dimensional rather than two dimensional ionosphere model is recommended to achieve better performance.
- 4) A fixed grid size was imposed on the ionosphere shell in this research, which is reasonable for small GPS networks. However, for a larger network, the grid size should be flexible to account for the different variation patterns in the directions of geomagnetic local hour angle and geomagnetic latitude.
- 5) In this thesis, the ionosphere was estimated after the ambiguities were resolved. The quality of the recovered ionosphere therefore relies, to a great extent, on the reliability of ambiguity resolution. Incorrect ambiguities will degrade the ionosphere estimates, and even cause the divergence of the estimation process. A superpower Kalman filter can be designed in the future, which is capable of estimating the ionosphere parameters and the ambiguities simultaneously.

- 6) There were no geomagnetic storms happening during the time when the data used in this thesis was collected. The ionosphere was quiet and the derived vertical TEC varies smoothly with time. Testing under a variety of ionospheric conditions is also preferred in the future in order to evaluate the performance of the proposed method.

REFERENCES

Black, H.D., and Eisner, A., Correcting Satellite Doppler Data for Tropospheric Effects, *Journal of Geophysical Research*, Vol. 89, 1984.

Braasch, M.S., Multipath Effects, in *Global Positioning System: Theory and Applications*, Vol. I, ed. B.W. Parkinson and J.J. Spilker, American Institute of Aeronautics and Astronautics, Washington, D.C., 1996.

Bugoslavskaya, N.Y., *Solar Activity and the Ionosphere, for Radio Communications Specialists*, Pergamon Press Ltd., New York, 1962.

Cander, L.R., Space Weather Effects on Telecommunication, *Second International Workshop on Artificial Intelligence Applications in Solar-terrestrial Physics*, Lund, 29-31 July, Sweden, Abstracts, pp. 5, 1997.

Cannon, M.E., High-accuracy GPS Semikinematic Positioning: Modelling and Results, *Navigation: Journal of the Institute of Navigation*, Vol. 37, No. 1, 1990.

Cannon, M.E., ENGO 561: *Satellite Positioning*, Department of Geomatics Engineering, The University of Calgary, Winter 1997.

Davies, K., *Ionospheric Radio*, Peter Peregrinus Ltd., London, 1989.

Department of Defense, *Global Positioning System Standard Positioning Service – Signal Specification*, 1993.

Duan, J.P., Bevis, M., Fang, P., Bock, Y., Chiswell, S., Businger, S., Rocken, C., Solheim, F., Hove, T.V., Ware, R., McClusky, S., Herring, T.A., and King, R.W., GPS

Meteorology: Direct Estimation of the Absolute Value of Precipitable Water, *Journal of Applied Meteorology*, Vol. 35, No. 6, June 1996.

El-Arini, M.B., O'Donnell, P.A., Kellam, P., Klobuchar, J.A., Wisser, T.C., and Doherty, P.H., The FAA Wide Area Differential GPS (WADGPS) Static Ionospheric Experiment, *Proceedings of the Institute of Navigation National Technical Meeting*, San Francisco, CA, January 1993.

El-Arini, M.B., Hegarty, C.J., Fernow, J.P., and Klobuchar, J.A., Development of an Error Budget for A GPS Wide-Area Augmentation System (WAAS), *Proceedings of The Institute of Navigation National Technical Meeting*, San Diego, CA, January 1994.

El-Arini, M.B., Conker, R., Albertson, T., Reegan, J.K., Klobuchar, J.A, and Doherty, P., Comparison of Real-time Ionospheric Algorithms for A GPS Wide-area Augmentation system (WAAS), *Navigation: Journal of the Institute of Navigation*, Vol. 41, No. 4, Winter 1994-1995, pp. 393-413.

Enge, P.K., and Van Dierendonck, A.J., Wide Area Augmentation System, in *Global Positioning System: Theory and Applications*, Vol. II, ed. B.W. Parkinson and J.J. Spilker, American Institute of Aeronautics and Astronautics, Washington, D.C., 1996.

Gao, Y., Heroux, P., and Kouba, J., Estimation of GPS Receiver and Satellite L1/L2 Signal Delay Biases Using Data from CACS, *Proceedings of KIS-94*, Banff, Canada, August 30 - September 2, 1994, pp. 109-117.

Gao, Y., Li, Z.F., and McLellan, J.F., Carrier phase Based Regional Area Differential GPS for Decimetre-Level Positioning and Navigation, *Proceedings of ION GPS-97*, The

10th International Technical Meeting of the Satellite Division of the Institute of Navigation, Kansas City, Missouri, September 16-19, 1997, pp. 1305-1313.

Gao, Y. and Li, Z.F., Ionosphere Effect and Modelling for Regional Area Differential GPS Network, *Proceedings of ION GPS-98*, The 11th International Technical Meeting of the Satellite Division of the Institute of Navigation, Nashville, Tennessee, September 15-19, 1998, pp. 91-97.

Georgiadou, Y., and Kleusberg, A., On the Effect of Ionospheric Delay on Geodetic Relative GPS Positioning, *Manuscripta Geodaetica*, 13, 1-8, 1988.

Georgiadou, Y., and Doucet, K.D., The Issue of Selective Availability, *GPS World*, September – October 1990, pp. 53-56.

Gosling, J. T., D. J. McComas, J. L. Phillips, and S. J. Bame, Geomagnetic Activity Associated with Earth Passage of Interplanetary Shock Disturbances and Coronal Mass Ejections, *Journal of Geophysical Research*, 96, 1991, 7831-7839.

Hargreaves, J.K., *The Solar-Terrestrial Environment*, Cambridge University Press, Cambridge, 1992.

Hay, C., and Wong, J., Tropospheric Delay Prediction at the Master Control Station, *GPS World*, January 2000.

Hedling, G. and Jonsson, B., New Developments in the SWEPOS Network, *Proceedings of ION GPS-96*, Kansas city, Missouri, September 17-20, 1996, pp. 1803-1808.

Hoffmann-Wellenhof, B., Lichtenegger, H. and Collins, J., *Global Positioning System: Theory and Practice*, Springer-Verlag, New York, Third edition, 1994.

Hopfield, H.S., Tropospheric Effect on Electromagnetically Measured Range: Prediction from Surface Weather Data, Applied Physics Laboratory, Johns Hopkins University, Baltimore, MD, July 1970.

IGS Central Bureau, *International GPS Service for Geodynamics 1996 Annual Report*, ed. Zumberge, J.F., Fulton, D.E. and Neilan, R.E., Jet Propulsion Laboratory, California Institute of Technology, Pasadena, California U.S.A., November 1997.

Kalafus, R.M., Vilcans, J., and Knable, N., Differential Operation of NAVSTAR GPS, *Navigation: Journal of The Institute of Navigation*, 1984.

Kalafus, R.M., Van Dierendonck, A.J., and Pealer, N.A., Special Committee 104 Recommendations for Differential GPS Service, *Navigation: Journal of The Institute of Navigation*, Vol. 33, No. 1, 1986.

Kee, C. and Parkinson, B.W., Wide Area Differential GPS (WADGPS): Future Navigation System, *IEEE Transactions on Aerospace and Electronic Systems*, Vol. 32, No. 2, April 1996.

Klobuchar, J.A., Bishop, G.J., and Doherty, P.H., Total Electron Content and L-Band Amplitude and Phase Scintillation Measurements in the Polar Cap Ionosphere, *AGARD-CPP-382*, May 1985.

Klobuchar, J.A., Ionospheric Time-Delay Algorithm for Single-Frequency GPS Users, *IEEE Transactions on Aerospace and Electronic Systems*, Vol. AES-23, No. 3, May 1987.

Klobuchar, J.A., Ionospheric Effects on GPS, in *Global Positioning System: Theory and Applications*, Vol. I, ed. B.W. Parkinson and J.J. Spilker, American Institute of Aeronautics and Astronautics, Washington, D.C., 1996.

Komjathy, A. and Langley, R., An Assessment of Predicted and Measured Ionospheric Total Electron Content Using A Regional GPS Network, *Proceedings of the ION GPS-96 National Technical Meeting*, Santa Monica, California, January 1996.

Kursinski, R., Monitoring the Earth's Atmosphere with GPS, *GPS World*, March 1994.

Lachapelle, G., Cannon, M.E. and Lu, G., High Precision GPS Navigation with Emphasis on Carrier Phase Ambiguity Resolution, *Marine Geodesy*, Vol. 15, No. 4, 1992, pp. 253-269.

Mannucci, A.J., Wilson, B.D., and Edwards, C.D., A New Method for Monitoring the Earth's Ionospheric Total Electron Content Using the GPS Global Network, *Proceedings of the ION GPS-93*, Salt Lake City, Utah, September 22-24, 1993, pp. 1323-1332.

Moritz, H., *Introduction to Interpolation and Approximation*, Lecture Notes of the Second International Summer School in the Mountains, Ramsau, Austria, August 23 – September 2, 1977.

Niell, A.E., Global Mapping Functions for the Atmosphere Delay at Radio Wavelengths, *Journal of Geophysical Research*, Vol. 101, No. B2, pp. 3227-3246.

Parkinson, B.W., History and Operation of NAVSTAR, the Global Positioning System, *IEEE Transactions on Aerospace and Electronic Systems*, Vol. 30, No. 4, October 1994.

Parkinson, B.W., GPS Error Analysis, in *Global Positioning System: Theory and Applications, Vol. I*, ed. B.W. Parkinson and J.J. Spilker, American Institute of Aeronautics and Astronautics, Washington, D.C., 1996.

Pi, X.Q., Nandi, S., Stowers, D.A., Marcin, M.R., Lindqwister, U.J., Reyes, M.J., Moore, A.W., Fort, D.N., and Klobuchar, J.A., Development of Ionospheric Scintillation Monitoring System Using Receivers of the IGS Global GPS Network, *the ION 55th Annual Meeting*, Cambridge, MA, 28-30 June 1999.

Raquet, J., Lachapelle, G., and Melgard, T.E., Test of A 400km × 600km Network of Reference Receivers for Precise Kinematic Carrier-phase Positioning in Norway. *Proceedings of ION GPS-98, The 11th International Technical Meeting of the Satellite Division of the Institute of Navigation*, Nashville, Tennessee, September 15-19, 1998, pp. 407-416.

Remondi, B.W., Extending the National Geodetic Survey Standard GPS Orbit Formats, National Information Center, Rockville, Maryland, NOAA Technical Report NOS 133, NGS 46, 1989.

Rishbeth, H., and Garriott, O.K., *Introduction to Ionospheric Physics*, Academic Press, Inc., New York, 1969.

Saastamoinen, J., Contributions to The Theory of Atmospheric Refraction, *Bulletin Géodésique*, No. 105, pp. 270-298; No. 106, pp. 383-397; No. 107, pp. 13-34, 1973.

Schaer, S., *Mapping and Predicting the Earth's Ionosphere Using the Global Positioning System*, Ph. D dissertation, Astronomical Institute, University of Bern, Switzerland, 1999.

Seeber, G., *Satellite Geodesy: Foundations, Methods, and Applications*, Walter de Gruyter, Berlin New York, 1993.

Skone, S., An Adaptive WADGPS Ionospheric Grid Model for the Auroral Region, *Proceedings of ION GPS-98*, The 11th International Technical Meeting of the Satellite Division of the Institute of Navigation, Nashville, Tennessee, September 15-19, 1998, pp. 185-194.

Skone, S., Wide Area Ionosphere Grid Modelling in the Auroral Region, UCGE Reports 20123, Department of Geomatics Engineering, The University of Calgary, December 1998.

Spilker Jr., J.J., Tropospheric Effects on GPS, in *Global Positioning System: Theory and Applications*, Vol. I, ed. B.W. Parkinson and J.J. Spilker, American Institute of Aeronautics and Astronautics, Washington, D.C., 1996.

Van Dierendonck, A.J., Fenton, P., and Ford, T., Theory and Performance of Narrow Correlator Spacing in a GPS Receiver, *the ION National Technical Meeting*, San Diego, 1992.

Varner, C. and Cannon, M.E., The Application of Multiple Reference Stations to the Determination of Multipath and Spatially Decorrelating Errors, *Proceedings of the National Technical Meeting of the Institute of Navigation*, pp. 323-333.

Wanninger, L., Effects of the Equatorial Ionosphere on GPS, *GPS World*, July 1993.

Wanninger, L., Real-time Differential GPS Error Modelling in Regional Reference Station Networks, *Proceedings of the International Association of Geodesy Symposia*,

vol. 118, *Advances in Positioning and Reference Frames*, Rio de Janeiro, Brazil, 1997, pp. 86-92.

Ware, R., GPS Sounding of Earth's Atmosphere, *GPS World*, 3, 1992, pp. 56- 57.

Ware, R. Exner, M., Feng, D., Gorbunov, M., Hardy, K., Herman, B., Kuo, Y., Meehan, T., Melbourne, W., Rocken, C., Schreiner, W., Sokolovskiy, S., Solheim, F., Zou, X., Anthes, R., Businger, S., and Trenberth, K., GPS Sounding of the Atmosphere from Low Earth Orbit: Preliminary Results, *Bulletin of the American Meteorological Society*, Vol. 77, No. 1, January 1996.

Wooden, W.H., Navstar Global Positioning System: 1985, *Proceedings of the First International Symposium on Precise Positioning with the Global Positioning System*, Rockville, Maryland, 1985.

Wu, B., Nicolaidis, P. and Upadhyay, T.N., Ionospheric Error Compensation for GPS Receivers Using Real-Time Ionospheric Model, *Proceedings of the ION GPS-96*, Kansas City, Missouri, September 1996.

Wübbena, G., Bagge, A., Seeber, G., Volker, B. and Hankemeier, P., Reducing Distance Dependent Errors for Real-time Precise DGPS Applications by Establishing Reference Station Networks, *Proceedings of the ION GPS-96*, Kansas City, Missouri, September 1996, pp. 1845-1852.